Electrical Engineering Technical Journal

# Electrical Engineering Technical Journal

ISSN: 3007- 9772
Vol. 3, No. 1, Jan. (2026)

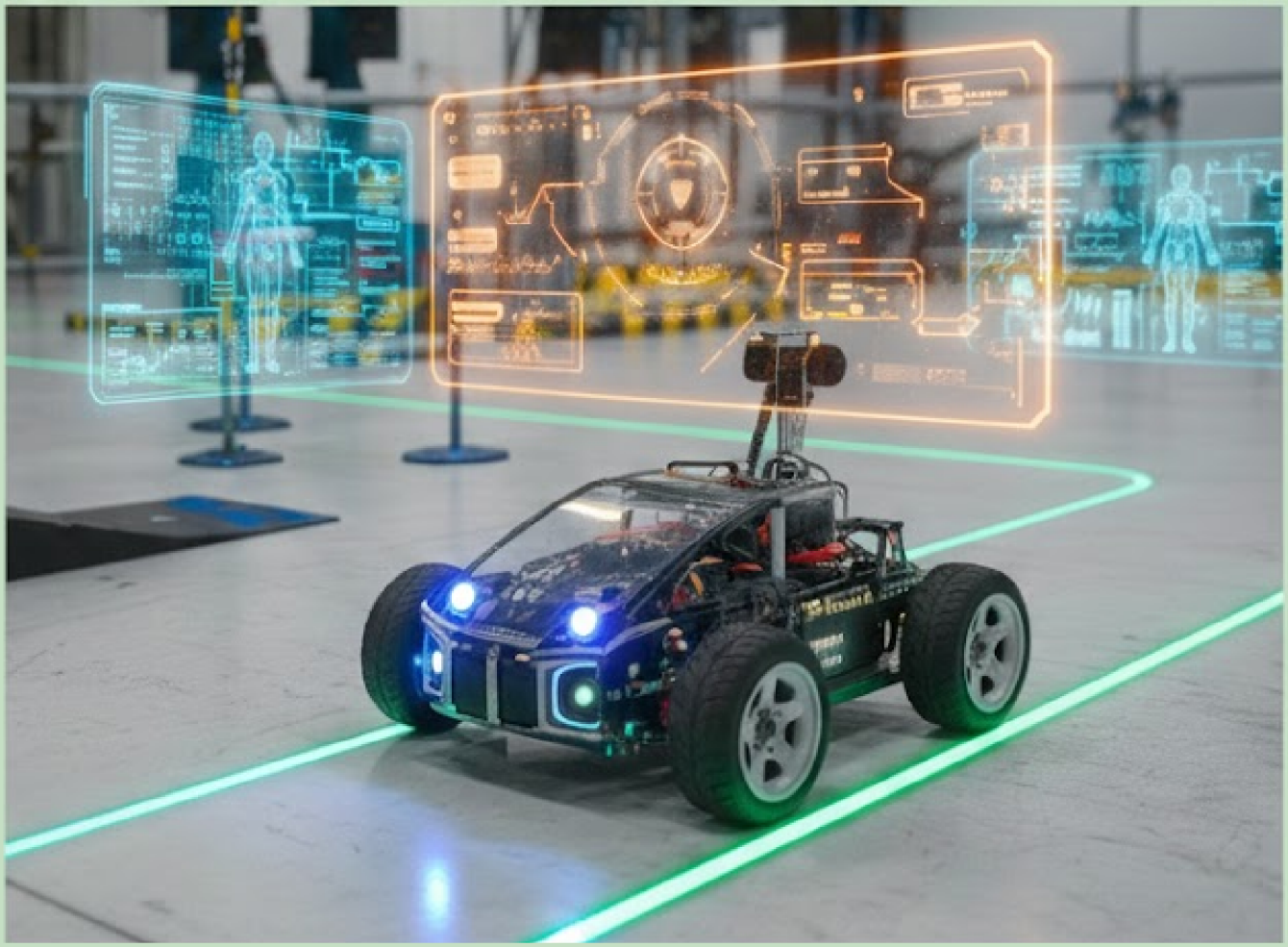

Deposit number in the House of Books and Documents in Baghdad 2751 for the year 2024

# Electrical Engineering Technical Journal

## Aim

The overarching aim of EETJ is to emerge as a pivotal catalyst for advancing the frontiers of knowledge in the dynamic realm of applied engineering. Our mission is to provide a distinguished platform that fosters rigorous research and facilitates the exchange of cutting-edge ideas, innovation, and best practices within the applied-engineering community and beyond. With commitment to excellence, EETJ aspires to contribute significantly to the evolution and practical implementation of applied engineering methodologies, technologies, and applications, particularly tailored to this field's unique challenges and opportunities. By bringing together a diverse spectrum of researchers, academics, and experts, EETJ aims to create a collaborative environment where the latest developments in data science can be explored and leveraged to address real-world challenges. Our journal seeks to be a beacon for transformative research, empowering individuals and organizations to harness the power of data-driven insights and technological advancements for societal and economic benefit. In addition, EETJ strives to disseminate high-quality scholarly contributions and cultivate a community that actively engages in interdisciplinary discourse, fostering the cross-pollination of ideas and expertise. Through this commitment, IJDS aims to play a pivotal role in shaping the trajectory of data science and related fields, ultimately contributing to the scientific landscape's growth, innovation, and sustainable development.

## Scope:

EETJ welcomes original research articles, reviews, and technical notes covering a wide spectrum of topics in applied engineering, including but not limited to:

- Electrical and Electronics Engineering: Network Technologies, Wireless Communication.
- Information Security, Artificial Intelligence in Computer and Communication Engineering, Cybersecurity and IT.
- Biomedical Engineering: Medical Imaging, Healthcare Technologies,
- Biomechanics, Artificial Intelligence in Medical Instrumentation and Biomedical Engineering.
- Control and System Engineering: Control Systems, Automation Technologies, Intelligent Unmanned Systems, Artificial Intelligence in Control and Automation Engineering.

# Editor-in-Chief

**Prof. Dr. Raed Abdul Hameed**

Bradford University, United Kingdom

---

# Members of Editorials Boards

Prof. Dr. Adel A. Obed, Middle Technical University, Iraq

Prof. Dr. Daniel Augusto Pereira, Universidade Federal de Lavras, Brazil

Prof. Dr. Mohamed Nasr, Tanta University, Egypt

Asst. Prof. Dr. Saif aldeen Saad Al-Kadhim, Xian Jiaotong University, China

Asst. Prof. Dr. Taha Ahmed Olaiwy, Ministry of Higher Education and Scientific Research, Iraq

Asst. Prof. Dr. Hayder Rafee Kareem, Kufa University, Iraq

Asst. Prof. Dr. Ayad Al-Dujaili, Middle Technical University, Iraq

Asst. Prof. Dr. Asnaka Perera, University of Southern Queensland, Australia

Asst. Prof. Dr. Abdulrahman Al-Shanoon, Ontario Tech University, Canada

Asst. Prof. Dr. Effariza Hanafi, University Malaya, Kuala Lumpur, Malaysia

Asst. Prof. Dr. Yaseein Soubhi Hussein, Ahmed Bin Mohammed Military College, Qatar

---

## Managing Editors & Technical Support

Prof. Dr. Ali Al-Naji, Adelaide University, Australia/ **Journal manager**

Asst. Prof. Osamah Sabah Barrak, University of Monastir, Monastir, Tunisia

Dr. Osama Abbas Hussein, Middle Technical University, Iraq

Mr. Mohammed Akeel Mohammed, Middle Technical University

---

## Copyediting and Proofreading

Asst. Prof. Dr. Oras A. Al-Ani, Middle Technical University, Iraq

Asst. Prof. Dr. Ali Mohammed Ali, Middle Technical University, Iraq

Mr. Husam H. Hasan, Middle Technical University, Iraq

# Index of Contents

Electrical Engineering Technical Journal, ISSN: 3007-9772, Vol. 3, No. 1, 2026, Pages 1-7
DOI: https://doi.org/10.51173/eetj.v3i1.29

*Electrical Engineering Technical Journal*
Journal homepage: http://eetj.mtu.edu.iq

*RESEARCH ARTICLE*

# $SiO_2/Al_2O_3/HfO_2$ Selective Buried Oxide Layer (SELBOX) Engineering and Its Influence on 20 nm n-MOSFET

**Aemen Qais A. Al-Yozbakee [1*], Qais Th. Algwari [1]**

[1] College of Electronics Engineering, Ninevah University, Mosul, Iraq

[*] Corresponding Author Email: aeman.qais.eng23@stu.uoninevah.edu.iq

**Article Info.**

Article history:

Received
24 July 2025

Accepted
8 October 2025

Published in Journal
5 December 2025

**Abstract**

Miniaturizing Metal Oxide Semiconductor Field Effect Transistors (MOSFETs) to the nanoscale results in specific structure and performance effects known as Short Channel Effects (SCEs). Performance degradation due to SCEs occurs due to increased leakage currents (IOFF), decreased threshold voltage ($V_{TH}$) stability and breakdown voltage. Various solutions for these problems have been developed through the application of structural and material engineering techniques. One particular engineering technique that shows promise as a potential solution is to incorporate a Selective Buried Oxide Layer (SELBOX). In this article, we investigate how the introduction of a SELBOX impacts the electrical characteristics of nano-scale n-MOSFETs through device simulation (TCAD). For the purposes of this study, we developed a 20 nm n-MOSFET with a high-k $HfO_2$ gate dielectric using the TCAD Silvaco ATLAS software package. Three different types of $SiO_2$, $Al_2O_3$, and $HfO_2$ dielectric materials were used in conjunction with the SELBOX layer which is located at a depth of 30 nm from the drain. In addition, the location of the SELBOX as related to the drain was also varied from its original position to the direct vicinity of the channel to assess the overall effect of the SELBOX position. Finally, we compare the characteristics of a conventional-type MOSFET (no SELBOX) to those of devices modified by inclusion of the SELBOX at varying positions/depths from the drain. The findings indicate that the dielectric constant and band gap of the implanted material, as well as its closeness to the drain and channel region, substantially influence device performance. In the instance of $SiO_2$ as SELBOX material, the $I_{OFF}$ decreased by 33%, and the breakdown voltage significantly increased from 85.09 V to 491.4 V. The utilization of $Al_2O_3$ resulted in a 27% reduction in $I_{OFF}$ and an increase in breakdown voltage from 85.09 V to 275.7 V. Notably, the application of $HfO_2$ as SELBOX material resulted in a divergent effect: $I_{OFF}$ rose by 21%, but the breakdown voltage increased to 172.3 V.

This is an open-access article under the CC BY 4.0 license (http://creativecommons.org/licenses/by/4.0/) Publisher: Middle Technical University

**Keywords:** $Al_2O_3$; $HfO_2$; n-MOSFET; SELBOX; Silvaco ATLAS; Breakdown Voltage.

## 1. Introduction

Integrated circuits rely heavily on the MOSFET as a result of its scalable nature, an economical price point and compatibility with CMOS processing technology [1]. The MOSFET is also utilised within the context of intelligent control systems [2], and during the process of creating efficient hybrid energy systems [3]. However, as channel lengths decrease towards nanoscale dimensions, short channel effects (SCEs), such as threshold voltage ($V_{TH}$) roll-off, drain-induced barrier lowering (DIBL) and increased leakage currents ($I_{OFF}$) begin to severely limit device performance and reliability. Therefore, these limitations require the creation of new solutions that provide electrostatic integrity, high drive current (ID) and minimal power consumption. Silicon-on-insulator (SOI) architectures and high-k gate dielectric materials have been proposed as some of the potential solution approaches. SOI MOSFETs utilize a buried oxide layer to diminish parasitic capacitance and leakage [4,5], although high-k materials like $Al_2O_3$ (k = 9, Eg = 8.8 eV) and $HfO_2$ (k = 25, Eg = 5.8 eV) are replacing traditional $SiO_2$ to facilitate additional scaling [6]. Although these methods have demonstrated efficacy, they mainly depend on global structural changes. Localized dielectric engineering has received insufficient attention, despite its potential to more effectively mitigate SCEs without the disadvantages associated with continuous buried oxides. Narayanan et al. [7] examined the kink effect in partially depleted SOI 2 µm MOSFETs and showed that the implantation of a 0.4 µm SELBOX structure beneath the source and drain efficiently mitigates the floating-body-induced kink. The work demonstrated using Silvaco ATLAS simulations that optimizing the length and thickness of the oxide gap diminishes the kink effect while maintaining the advantages of SOI, with a created device model offering more insights into the optimization of SELBOX parameters. Thakral et al. [8] examined the scaling difficulties of 28 nm SOI MOSFETs and discovered planar fully depleted SOI (FD-SOI) as an appropriate low-power substitute for bulk CMOS. Their TCAD-based research shown that the kink effect in partially depleted SOI (PD-SOI) devices may be effectively mitigated with the implementation of a 0.4 µm SELBOX structure, hence improving device reliability while maintaining the fundamental advantages of SOI technology. Narayanan et al. [9] introduced an enhanced 0.12 µm SOI MOSFET architecture using a 100 nm SELBOX beneath the source and drain to reduce self-heating issue. TCAD simulations validated that adjusting gap parameters significantly mitigates thermal effects while maintaining SOI performance advantages. Mahmoud et al. [10] constructed a 90 nm CMOS employing a 10 nm SELBOX via TCAD ATLAS and assessed the dynamic power relative to SOI CMOS and BULK CMOS. The total dissipated dynamic power across all individuals is equivalent at elevated frequencies. The dynamic power dissipation of the SOI and SELBOX structures was similar at low frequencies, both demonstrating lower

values than the BULK configuration. SELBOX CMOS eliminated the kink effect and self-heating, making it superior than SOI CMOS. The SELBOX MOSFET improves device efficiency by reducing power loss. Yoo and Kim [11] introduced a 45 nm buried oxide with a Buried Oxide Nano-sheet Field Effect Transistor (BO-NSFET) that situates the oxide exclusively beneath the gate region to mitigate substrate band-to-band tunneling (BTBT). According to TCAD studies, the proposed design provides a substantial reduction in IOFF and parasitic leakage versus traditional NSFETs allowing for improved performance at advanced nodes. Additionally, Murshid and Bashir [12] proposed a GP-SELBOX Junction Less Transistor to address the limitations of conventional SOI-JLTs operating at less than 20 nm nodes. The addition of a p-type ground plane and a 10 nm SELBOX to the device structure provides greater depletion, reduced leakage, improved ION/IOFF ratio, better SCE management while maintaining comparable cutoff frequency and less self-heating.

This research demonstrates how newly designed layers of SELBOX layer engineering for nanoscale MOSFETs can optimize performance through material choice and vertical positioning of the dielectric material layer. The study also demonstrates that using a high band gap dielectrics material such as $SiO_2$ in the near channel-drain junction location, will reduce leakage current by as much as 33%, and increase the breakdown voltage over five times compared to the conventional designs. Results indicate that $Al_2O_3$ provides a moderate improvement in performance, while $HfO_2$ demonstrates the limitations of using lower bandgap dielectrics material in the same position. These results point to an important new avenue of investigation: the interaction between buried dielectric materials properties and their spatial position has the potential to create new options for optimization of device performance in advanced technology nodes with short channels.

## 2. Methodology

This study employs TCAD Silvaco ATLAS to model and study an n-channel MOSFET at the nanoscale. The W/L ratio of this structure is 100 nm/20 nm. Use of a high-k gate dielectric such as $HfO_2$ also helps to achieve low gate leakage characteristics of this device while maintaining excellent electrostatic control of the channel, as shown in Table 1 which lists the primary parameters investigated by [8].

**TABLE 1.** Parameters of design 20 nm n-MOSFET.

| Parameters | Value |
|---|---|
| Channel | 20 nm Si |
| Doping of Source and Drain | $5 \times 10^{20}\ cm^{-3}$ |
| Doping of Channel | $9 \times 10^{17}\ cm^{-3}$ |
| Doping of Substrate | $1 \times 10^{14}\ cm^{-3}$ |
| Gate Workfunction | 4.55ev |
| Gate length | 25 nm |
| Source and Drain Length | 40 nm |
| Gate Dielectric Thickness | 10 nm |

Correct model selection is critical in the structure of this simulation. In this work, the Auger (three carriers) and SRH (fixed minority carrier lifetime) models are used for the direct transitions. The Arora Model replaces the ANALYTIC model for Si, and the CVT method applies to the overall system. The numerical solver, Newton-Gummel with trap autonr, gives consistently better starting estimates compared to more complex situations.

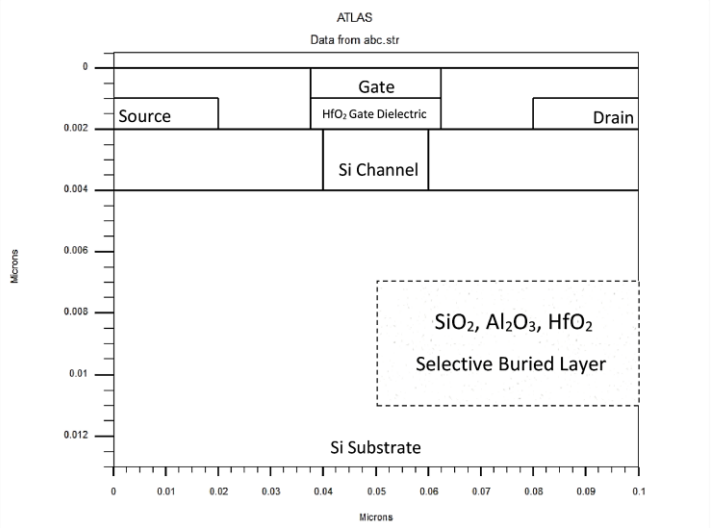


**Fig. 1.** Schematic View of insertion selective buried oxide layer (SELBOX) in 20 nm n-MOSFET.

The selective oxide layer (SELBOX) for our research is a crucial component and is located within the silicon substrate. At a thickness of 40nm and located at 30nm, the SELBOX extends from 50nm to 100nm in the lateral dimension along the x-axis. Three distinct dielectric materials are utilized independently for the SELBOX in different models: $SiO_2$, $Al_2O_3$, and $HfO_2$ as shown in Figure 1. This facilitates a comparative assessment of the impact of each dielectric material and band gap value on the device concerning SCEs. In succeeding modeling, the SELBOX is elevated in the upward direction until it achieves direct contact with the active channel region. The use of various materials and vertical repositioning is conducted to assess how the closeness of the SELBOX to the channel affects electric field distributions and whole device performance.

## 3. Results and Discussion

### *3.1. $SiO_2$ material (k=3.9 and band gap=9 eV)*

This study assesses the electrical properties of 20 nm n-MOSFET devices with $SiO_2$ SELBOX depths of 30 nm, 20 nm, 10 nm, and direct contact position with the channel, in comparison to a standard design of 20 nm n-MOSFET (without a SELBOX). The primary parameters evaluated comprise threshold voltage ($V_{TH}$), ON current ($I_{ON}$), OFF current ($I_{OFF}$), $I_{ON}/I_{OFF}$ ratio, breakdown voltage, and Drain-Induced Barrier Lowering (DIBL).

Table 2 illustrates that the $V_{TH}$ exhibits remarkable stability across all SELBOX positions, with minimal variations from 0.462 V in the standard design to 0.461 V in the direct contact position, that means the substrate coupling not affected, in order to the electrostatics in the channel stay steady. The slight fluctuation indicates that the vertical placement of the $SiO_2$ SELBOX minimally affects the $V_{TH}$, which is beneficial for preserving device switching stability.

**TABLE 2.** Main parameters of (standard design of n-MOSFET) and the influence of $SiO_2$ selective buried oxide layer (SELBOX) at (30 nm depth, 20 nm depth, 10 nm depth and direct contact position).

| Parameters | Standard | 30 nm Depth | 20 nm Depth | 10 nm Depth | Direct Contact |
|---|---|---|---|---|---|
| $V_{TH}$ (V) | 0.462 | 0.454 | 0.456 | 0.458 | 0.461 |
| $I_{ON} \times 10^{-3}$ (A/m) | 2 | 2.12 | 2.11 | 2.10 | 2.07 |
| $I_{OFF} \times 10^{-11}$(A/m) | 8.5 | 10 | 8.89 | 7.24 | 5.68 |
| $I_{ON}/I_{OFF} \times 10^{7}$ | 2 .37 | 1.98 | 2.37 | 2.90 | 3.65 |
| Breakdown Voltage (V) | 85.09 | 137.1 | 199.3 | 312.5 | 491.4 |
| DIBL (mV/V) | 308 | 307 | 306 | 304 | 302 |

The $I_{ON}$ exhibits a little fluctuation with alterations in SELBOX depth. Raising the SELBOX depth from 30 nm to 10 nm improves electrostatic gate control over the channel, elevating $I_{ON}$ from $2.00 \times 10^{-3}$ A/m in the standard design to $2.12 \times 10^{-3}$ A/m at 30 nm depth. When the SELBOX is in direct contact with the channel, $I_{ON}$ diminishes to $2.07 \times 10^{-3}$ A/m, indicating a decline in effective gate control caused by the modified field distribution inside the device's bulk [14].

Conversely, the $I_{OFF}$ has a greater degree of fluctuation. The implanting of a SELBOX at a depth of 30 nm elevates $I_{OFF}$ from $8.5\times10^{-11}$ A/m at standard design to $1.0\times10^{-10}$ A/m at 30 nm depth. The improved performance of the fringing fields around the source/drain regions and additional junction leakage due to their physical distance from the substrate explains the increase in performance. In particular, the decrease in the drain-source-off current ($I_{OFF}$) to $5.68 \times 10^{-11}$ A/m due to improved isolation and reduction in leakage paths from the substrate (the SELBOX is placed in direct contact) is another example of the benefits of using this configuration [15].

The $I_{ON}/I_{OFF}$ ratio significantly enhances, attaining $3.65 \times 10^{7}$ in the direct contact position, in contrast to $2.37 \times 10^{7}$ in the standard MOSFET. This illustrates exceptional switching performance and indicates that the revised SELBOX positioning improves the equilibrium between $I_{ON}$ performance and $I_{OFF}$ mitigation. A significant enhancement is noted in the breakdown voltage, rising from 85.09 V in the standard design to 491.4 V upon direct contact of the SELBOX with the channel. This improvement results from the diminished fringing fields at the drain side, coupled with the high bandgap (about 9 eV) of $SiO_2$ and its insulating barrier effect, which decreases the vertical electric field within the substrate and enhances dielectric robustness. As a result, leakage is further reduced, and the MOSFET attains markedly improved dependability [16] [17].

Throughout all configurations, the DIBL values are approximately 306 mV/V indicating that the placement of the $SiO_2$ SELBOX is more important in terms of leakage and breakdown character than it is for electrostatic stability.

As illustrated in Figure 2, there is a distribution of electric fields from the placement of the $SiO_2$ SALBOX, which causes an increase in the fringing electric field at the source side at 30 nm down from the surface of the device compared to the large amount of fringing electric field present at the drain side. This is because the oxide layer prohibits the passage of electric fields through it, this results in perturbing the potential distribution throughout the monolithic device, as it will bend upwards towards the area of electric field concentration.

Moreover, the density of the field lines above the buried oxide layer is substantially less than the field lines below the oxide layer. This phenomenon can be attributed to the shielding—or partially shielding—effect of the buried oxide.

As the SELBOX is raised from a depth of 30 nm to a direct contact position beneath the drain region, the field distribution exhibits significant enhancements. The source side fringing fields have diminished, and the SELBOX now functions as a more robust barrier against electric field entry into the substrate, efficiently directing and reducing substrate coupling. At the drain side, the electric field intensity at the drain-substrate interface becomes higher, while the oxide isolation considerably diminishes field entry into the bulk silicon, therebyavoiding early breakdown of the device. The enhanced field confinement results in a significant rise in breakdown voltage, as verified by Table 2, which shows breakdown voltage rising from 85.09 V in the standard design to 491.4 V with direct contact to the SELBOX.

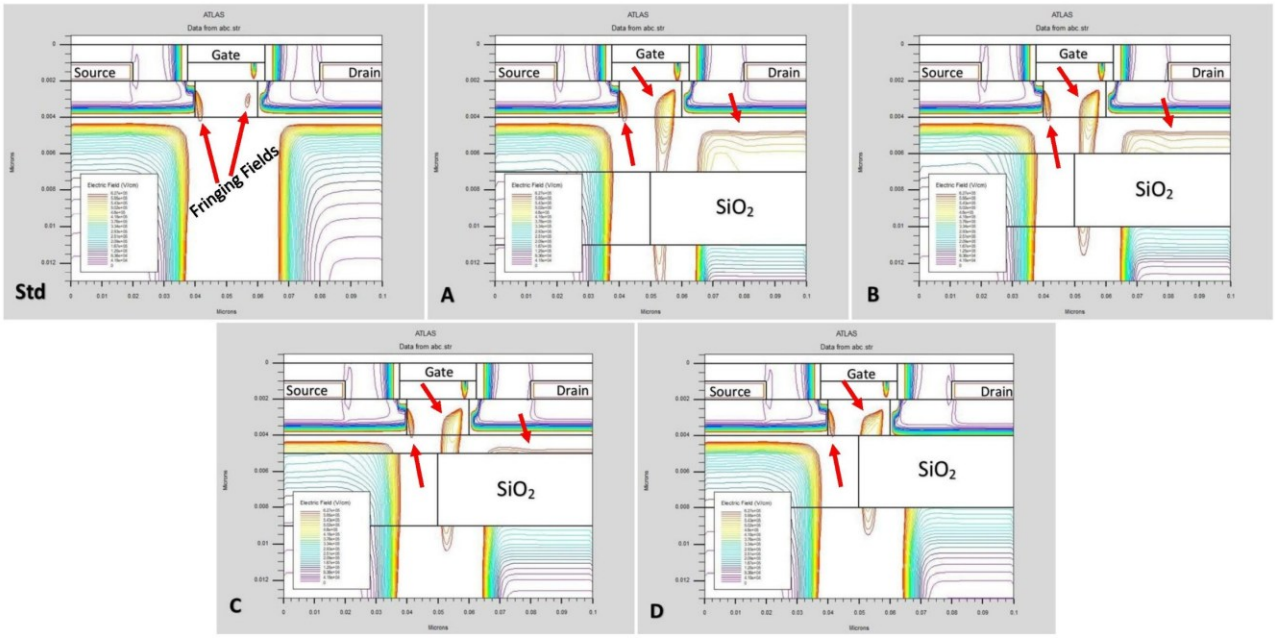


**Fig. 2.** Electric field distribution at (standard design of n-MOSFET) and $SiO_2$ selective buried oxide layer (SELBOX) at (30 nm depth, 20 nm depth, 10 nm depth and direct contact position).

### *3.2. $Al_2O_3$ material (k=9 and band gap=8.8 eV)*

This investigation assesses the performance of MOSFET devices utilizing $Al_2O_3$ as the SELBOX at depths of 30 nm, 20 nm, 10 nm, and in direct contact with the channel, in comparison to a conventional design.

The data presented in Table 3 displays strong stability of the $V_{TH}$ value in each of the different types of SELBOX designs, with the $V_{TH}$ fluctuating, but only by 0.003 V, between 0.461 and 0.464 across the various designs. Therefore, it can be concluded that the use of $Al_2O_3$ for the SELBOX does not negatively impact the electrostatics of the channel or the amount of control exerted by the gate over the channel. In addition, the high dielectric constant value (K = 9) for $Al_2O_3$ provides superior gate-to-channel modulation and also minimizes the effects of SCE. Therefore, the stability of the VTH demonstrates that $Al_2O_3$ can provide the necessary reliable switching performance in modern CMOS designs.

In terms of $I_{ON}$ performance, the values for ION are stable and robust throughout the range of designs with only minor fluctuations as compared to the standard design. At all depths of SELBOX, including the depth of direct contact between the SELBOX and the substrate, the value of $I_{ON}$ for the $Al_2O_3$ SELBOX was recorded at $2\times10^{-3}$ A/m. The data indicates that the high dielectric constant of $Al_2O_3$ provides adequate electrostatic gate control; therefore, when the oxide layer is positioned closer to the drain, the electrostatic force produced will keep the inverter inversion due to charge response for the $Al_2O_3$ oxide intact. In contrast to the $Al_2O_3$ findings, the $SiO_2$ SELBOX had a slight decrease in the value of ION when the oxide was in direct contact with the substrate, indicating that the $Al_2O_3$ has a greater ability to maintain a strong inversion charge density and ION capability.

As the SELBOX is elevated from 30 nm deep ($8.52 \times 10^{-11}$ A/m, the $I_{OFF}$ drops to $6.20 \times 10^{-11}$ A) to the point of direct contact, the $I_{OFF}$ decreases. This increase in performance occurs because of decreasing fringing electric fields in the space adjacent to the drain junction, and the increased physical separation of leakage paths between the source/drain and substrate. The $I_{ON}/I_{OFF}$ ratio markedly increases from $2.37 \times 10^7$ in the standard design to $3.24 \times 10^7$ upon direct contact position, indicating enhanced switching efficiency with minimal reduction in $I_{ON}$.

Compared to a standard SELBOX design of 85.09 V based on traditional dielectric materials and structures, the breakdown voltage increases significantly from 85.09 V to 275.7 V with a device constructed using improved technology to create a direct contact position. The increased breakdown voltage is attributed to the high-k material used, which is the $Al_2O_3$ insulation layer, allowing for a lower leakage of vertical electric fields into the substrate and improving the insulation between junctions. While $Al_2O_3$ has an energy band gap of approximately 8.8 eV, which is slightly lower than that of $SiO_2$ (approximately 9 eV), it can still effectively reduce high-field stress and prevent leakage from junctions. However, while the increase in breakdown voltage compared to devices created using $SiO_2$ based configurations is only slight, this indicates the importance of the trade-off between dielectric material band gap and dielectric permittivity when designing dielectric structures. Although $Al_2O_3$ provides a small reduction in leakage compared to $SiO_2$, it provides a substantial increase in breakdown voltage; however, it does not provide the same level of increase as $SiO_2$ based SELBOX designs. DIBL remains approximately consistent at 308 mV/V across all configurations, indicating that variations in SELBOX position and oxide material selection predominantly influence leakage and breakdown performance rather than the integrity of electrostatic gate channel control.

**TABLE 3.** Main parameters of (standard design of n-MOSFET) and the influence of $Al_2O_3$ selective buried oxide layer (SELBOX) at (30 nm depth, 20 nm depth, 10 nm depth and direct contact position).

| Parameters | Standard | 30 nm Depth | 20 nm Depth | 10 nm Depth | Direct Contact |
|---|---|---|---|---|---|
| $V_{TH}$ (V) | 0.462 | 0.461 | 0.462 | 0.463 | 0.464 |
| $I_{ON} \times 10^{-3}$ (A/m) | 2 | 2.03 | 2.03 | 2.02 | 2.01 |
| $I_{OFF} \times 10^{-11}$(A/m) | 8.5 | 8.52 | 7.97 | 7.25 | 6.20 |
| $I_{ON}/I_{OFF} \times 10^7$ | 2 .37 | 2.38 | 2.53 | 2.79 | 3.24 |
| Breakdown Voltage (V) | 85.09 | 130.5 | 155.7 | 198.7 | 275.7 |
| DIBL (mV/V) | 308 | 308 | 307 | 307 | 306 |

Figure 3 depicts the alterations in the electric field profile resulting from the relocation of the $Al_2O_3$ SELBOX. At a depth of 30 nm, the SELBOX induces a minor enhancement of fringing fields on the drain side, attributable to localized field crowding near the drain junction. As the SELBOX is elevated nearer to the drain, surrounding fields diminish consistently, exhibiting substantial suppression at the position of direct contact. The electric field scattering over the $Al_2O_3$ SELBOX is practically eliminated, illustrating the oxide's excellent insulating capability.

By reallocating electric field lines, the overall durability of electric field devices increases since vertical electric field penetration into the substrate is reduced. As a result, the amount of leakage path through the substrate is decreased and additional electric breakdown voltage is created. Dual gate (also known as $Al_2O_3$ relaxed dielectric) SELBOX can maintain minimal values of IOFF without compromising electric field confining effect. Therefore, this facilitates the use of electric field devices in scaled MOSFET architectures where oxide engineering plays a critical role in the maximization of ION, IOFF, and device reliability.

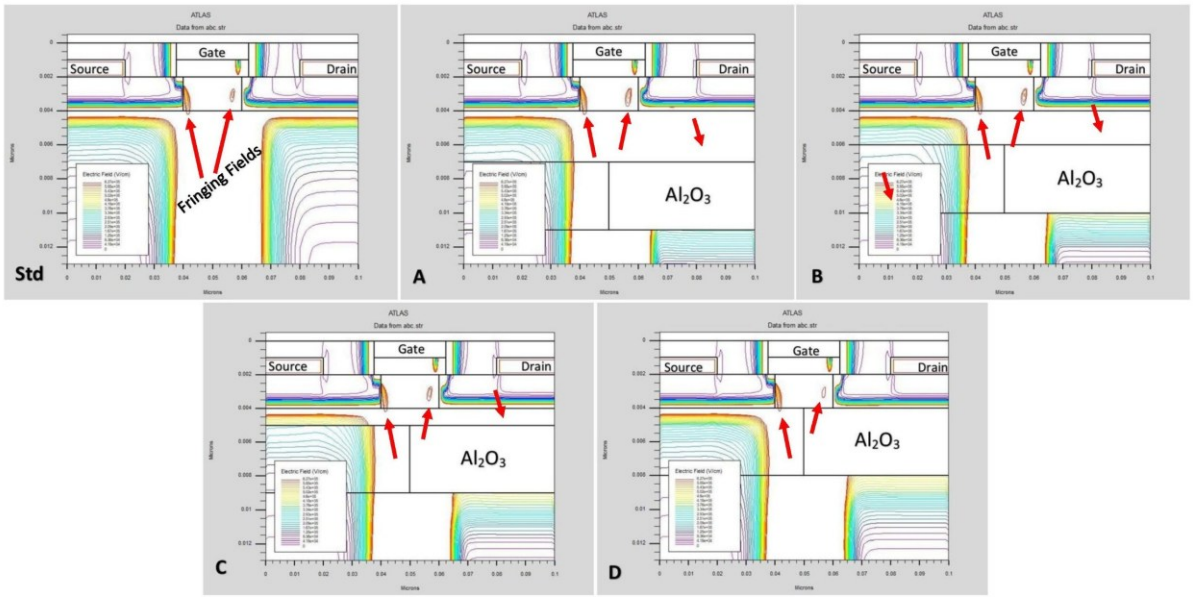


**Fig. 3.** Electric field distribution at (standard design of n-MOSFET) and $Al_2O_3$ selective buried oxide layer (SELBOX) at (30 nm depth, 20 nm depth, 10 nm depth and direct contact position).

### *3.3. $HfO_2$ material (k=25 and band gap=5.8 eV)*

This section examines the influence of different $HfO_2$ SELBOX depths 30 nm, 20 nm, and 10 nm, along with a direct contact configuration, on the performance of MOSFET devices, compared to a standard design of MOSFET device.

Table 4 depicts that the $V_{TH}$ exhibits a slight elevation with the implementation of the $HfO_2$ SELBOX, increasing from 0.462 V in the standard design to a peak of 0.470 V when the SELBOX is situated 30 nm beneath the drain region. The increase results from improved electrostatic confinement and less substrate coupling facilitated by the high-k $HfO_2$ layer, which reduces gate control over the channel at intermediate depths. As the SELBOX is elevated nearer to direct contact with the drain, $V_{TH}$ marginally lowers to 0.464 V. This reduction signifies that, although $HfO_2$ improves vertical isolation, its closeness to the channel somewhat modifies the electric field distribution and diminishes gate-to-channel electrostatics, resulting in a modest decrease in $V_{TH}$ [18].

The $I_{ON}$ values are marginally diminished in comparison to the standard MOSFET structure with $2.00 \times 10^{-3}$ A/m. The values fluctuate between $1.93 \times 10^{-3}$ A/m and $1.97 \times 10^{-3}$ A/m across all structures. The decrease is ascribed to the elevated dielectric constant and physical thickness of the SELBOX, which marginally diminishes inversion charge density and channel mobility by altering vertical electric fields. The little decrease in $I_{ON}$ suggests that the integration of $HfO_2$ SELBOX entails a compromise in $I_{ON}$ performance.

The $I_{OFF}$ demonstrates a nonlinear pattern. Initially, it diminishes to $7.44 \times 10^{-11}$ A/m at a SELBOX depth of 30 nm, due to diminished substrate coupling and efficient obstruction of leakage pathways. As the SELBOX approaches direct contact, $I_{OFF}$ increases to $10.3 \times 10^{-11}$ A/m, attributed to improved field penetration through the reduced substrate regions and leakage pathways along the SELBOX peripheries.

The $I_{ON}/I_{OFF}$ ratio exhibits a trend, reaching a maximum of $2.61 \times 10^7$ at a depth of 30 nm, exceeding the standard design of $2.37 \times 10^7$, before decreasing to $1.91 \times 10^7$ upon direct contact position. The results indicate that a 30 nm SELBOX depth optimally suppresses leakage while sustaining acceptable $I_{ON}$ levels, whereas direct contact, while enhancing breakdown voltage, and increases $I_{OFF}$.

$HfO_2$ SELBOX creates a drastic increase in the breakdown voltage through contact with $HfO_2$, going from the typical 85.09 V in design mode to 172.3 V in the direct contact mode. This increase is due to the larger dielectric constant of $HfO_2$ and the physical barrier to vertical electric field strength in the bulk substrate that results in the stability of $HfO_2$ devices. When compared with $SiO_2$ SELBOX devices, it should also be noted that $HfO_2$ has a lower bandgap (around 5.8 eV versus 9 eV), which limits the increase in maximum breakdown voltage, and thus, results in an increased IOFF, particularly when the oxide is positioned near the Drain region.

DIBL exhibits relative stability across all SELBOX depths at around 312 mV/V, indicating that although the selection and positioning of SELBOX materials significantly affect leakage and breakdown properties, electrostatic channel management remains uniform.
$7.44 \times 10^{-11}$ A/m at a SELBOX depth of 30 nm, subsequently rising to $10.3 \times 10^{-11}$ A/m as the SELBOX's direct contact position is altered. This increase is attributed to the SELBOX facilitating leakage pathways between the source and drain regions and the substrate. The $I_{ON}/I_{OFF}$ ratio attains its maximum at a depth of 30 nm, measuring $2.61 \times 10^7$, above the conventional design value of $2.37 \times 10^7$. However, it progressively decreases as the SELBOX is moved to the direct contact position, ultimately reaching $1.91 \times 10^7$. In comparison to the conventional MOSFET design, the breakdown voltage increases from 85.09 V to 172.3 V when a SELBOX is implanted at the direct contact location. The SELBOX first increases the breakdown voltage by creating an insulating barrier that reduces the vertical electric field in the bulk substrate. When the value of the band gap value became half of the band gap in first case, about 5.8 eV, and becoming closer

to the drain region, leading to a slight increment in the breakdown voltage, and an increase in the leakage current. DIBL values almost constant for all cases is approximately about 312 mV/V.

**TABLE 4.** Main parameters of (standard design of n-MOSFET) and the influence of $HfO_2$ selective buried oxide layer (SELBOX) at (30 nm depth, 20 nm depth, 10 nm depth and direct contact position).

| Parameters | Standard | 30 nm Depth | 20 nm Depth | 10 nm Depth | Direct Contact |
|---|---|---|---|---|---|
| $V_{TH}$ (V) | 0.462 | 0.470 | 0.468 | 0.466 | 0.464 |
| $I_{ON} \times 10^{-3}$ (A/m) | 2 | 1.94 | 1.95 | 1.93 | 1.97 |
| $I_{OFF} \times 10^{-11}$(A/m) | 8.5 | 7.44 | 8.76 | 10 | 10.3 |
| $I_{ON}/I_{OFF} \times 10^{7}$ | 2 .37 | 2.61 | 2.22 | 1.95 | 1.91 |
| Breakdown Voltage (V) | 85.09 | 111.6 | 109.1 | 125.3 | 172.3 |
| DIBL (mV/V) | 308 | 311 | 312 | 314 | 314 |

Figure 4 clarifies the characteristics of the electric field. The integration of $HfO_2$ SELBOX at a depth of 30 nm markedly diminishes fringing fields adjacent to the drain side, while the high-k shielding action of the oxide effectively obstructs field lines above the SELBOX. As the SELBOX approaches direct contact with the drain, the confinement of the electric field enhances, resulting in less vertical field penetration into the substrate. Nevertheless, robust localized electric fields develop within the SELBOX layer, aligning with the noted rise in $I_{OFF}$. This indicates that although $HfO_2$'s elevated dielectric constant enhances isolation, its reduced bandgap renders it more vulnerable to field-assisted leakage mechanisms in comparison to $SiO_2$ or $Al_2O_3$ SELBOX.

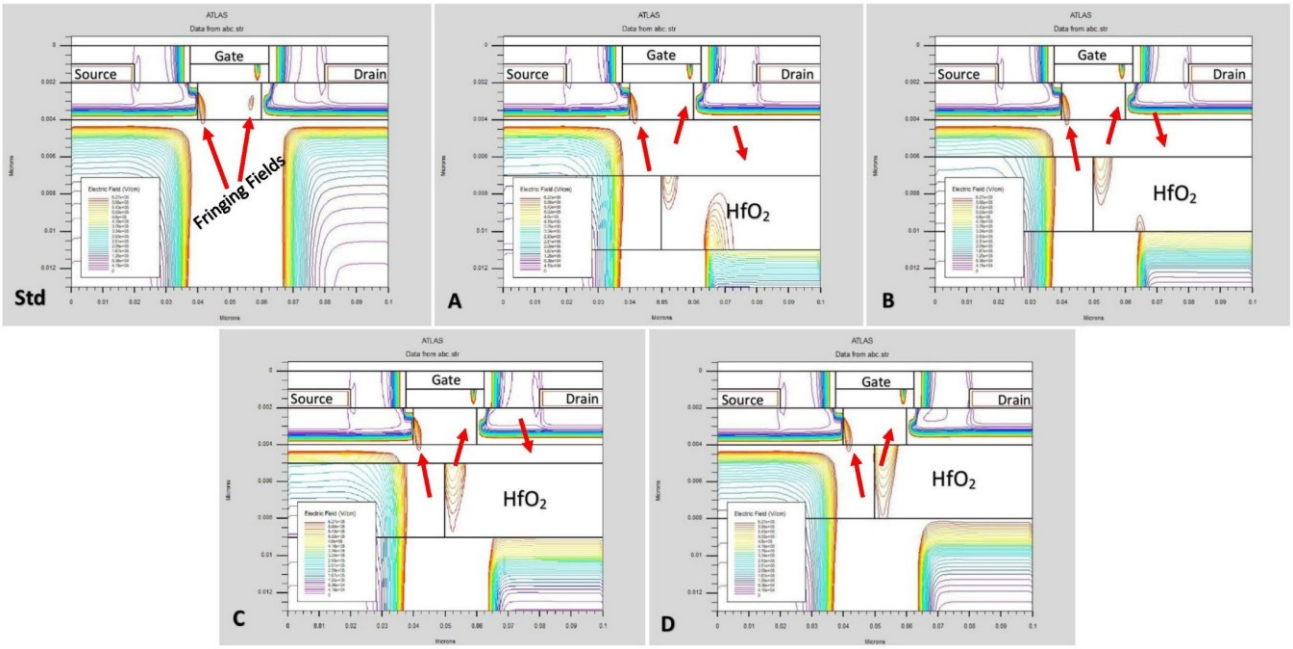


**Fig. 4.** Electric field distribution at (standard design of n-MOSFET) and $HfO_2$ selective buried oxide layer (SELBOX) at (30 nm depth, 20 nm depth, 10 nm depth and direct contact position).

## 4. Conclusion

Implanting a SELBOX beneath of drain region with three different materials, $SiO_2$, $Al_2O_3$, and $HfO_2$, with energy gaps of 9 eV, 8.8 eV, and 5.8 eV, respectively. The value of energy gap of materials and its closeness to drain region determines the average increasing and decreasing value of leakage current and breakdown voltage, as the SELBOX positioning from 30 nm depth to direct contact, it was noticed when the high value of band gap, such $SiO_2$ with 9 eV, and become more close to the drain-substrate contact, the leakage current is exponentially decreased by 17%, and the breakdown voltage is exponentially increased by 52%. When the band gap is slightly decreased, such as $Al_2O_3$ with 8.8 eV, the leakage current is slightly exponentially decreased by 10%, and the breakdown voltage is exponentially increased by 29%. Finally, the significant decrease in the value of band gap, such as $HfO_2$ with 5.8 eV, the leakage current is exponentially increased by 17%, and the breakdown voltage is exponentially increased by 16%. It was concluded that the material with a higher value of the band gap and closer to the drain region gives better results. Future research can extend this work in several directions, like exploring alternative high-k and ultra-wide band gap dielectrics such as $ZrO_2$, $La_2O_3$, or $Ga_2O_3$ as SELBOX layers could provide further insights into material-dependent performance. Another future approach, applying the concept of buried dielectric engineering to advanced device architectures, including FinFETs, Gate-All-Around (GAA) FETs, and nanosheet transistors, may reveal its scalability to beyond-20 nm nodes.

## References


[1] M. Aditya, K. S. Rao, B. Balaji, and K. G. Sravani, "Comparison of drain current characteristics of advanced MOSFET structures-a review," *Silicon,* vol. 14, no. 14, pp. 8269-8276, 2022. https://doi.org/10.1007/s12633-021-01638-8

[2] R. H. Ahmed and A. S. Nouri, "Enhanced Transient Stability in Power Systems via Intelligent Control of SVCs Using Neural Networks," *Electrical Engineering Technical Journal,* vol. 2, no. 2, pp. 17-24, 2025. https://doi.org/10.51173/eetj.v2i2.23

[3] S. M. Ferhan and H. Agahi, "Multi-Objective Optimization of Hybrid Energy Systems," *Electrical Engineering Technical Journal,* vol. 2, no. 2, pp. 1-16, 2025. https://doi.org/10.51173/eetj.v2i2.22

[4] K. Pradhan, P. Agarwal, P. Sahu, and S. Mohapatra, "Role of high-k materials in Nanoscale TM-DG MOSFET: A simulation study," *Invertis Journal of Science & Technology,* vol. 6, no. 4, pp. 195-199, 2013.

[5] B. Majkusiak, T. Janik, and J. Walczak, "Semiconductor thickness effects in the double-gate SOI MOSFET," *IEEE Transactions on Electron Devices,* vol. 45, no. 5, pp. 1127-1134, 2002. https://doi.org/10.1109/16.669563

[6] H. Yu *et al.*, "Energy gap and band alignment for (HfO 2) x (Al 2 O 3) 1− x on (100) Si," *Applied Physics Letters,* vol. 81, no. 2, pp. 376-378, 2002. https://doi.org/10.1063/1.1492024

[7] M. Narayanan, H. Al-Nashash, B. Mazhari, D. Pal, and M. Chandra, "Analysis of kink reduction in SOI MOSFET using selective back oxide structure," *Active and Passive Electronic Components,* vol. 2012, no. 1, p. 565827, 2012. https://doi.org/10.1155/2012/565827

[8] B. Thakral, G. Bakshi, and A. K. Kushwaha, "A review on SOI MOSFET and kink reduction using selective back oxide structure," in *2014 International Conference on Reliability Optimization and Information Technology (ICROIT)*, 2014: IEEE, pp. 487-490. https://doi.org/10.1109/ICROIT.2014.6798372

[9] M. Narayanan and H. Al Nashash, "Minimization of self-heating in SOI MOSFET devices with SELBOX structure," in *2016 11th International Conference on Advanced Semiconductor Devices & Microsystems (ASDAM)*, 2016: IEEE, pp. 61 https://doi.org/10.1109/ASDAM.2016.7805895

[10] R. Mahmoud, N. Madathumpadical, and H. Al-Nashash, "TCAD simulation and analysis of selective buried oxide MOSFET dynamic power," *Journal of Low Power Electronics and Applications,* vol. 9, no. 4, p. 29, 2019. https://doi.org/10.3390/jlpea9040029

[11] S. Yoo and S. Kim, "Leakage optimization of the buried oxide substrate of nanosheet field-effect transistors," *IEEE Transactions on Electron Devices,* vol. 69, no. 8, pp. 4109-4114, 2022. https://doi.org/10.1109/TED.2022.3182300

[12] M. Murshid and F. Bashir, "Ground plane and selective buried oxide based planar junctionless transistor," *Frequenz,* vol. 76, no. 1-2, pp. 1-7, 2022. https://doi.org/10.1515/freq-2021-0059

[13] V. P. Tayade and S. L. Lahudkar, "Implementation of 20 nm graphene channel field effect transistors using silvaco TCAD tool to improve short channel effects over conventional MOSFETs," *Advances in Technology Innovation,* vol. 7, no. 1, pp. 18-29, 2021. https://doi.org/10.46604/aiti.2021.8098

[14] J.-T. Park and J.-P. Colinge, "Multiple-gate SOI MOSFETs: device design guidelines," *IEEE transactions on electron devices,* vol. 49, no. 12, pp. 2222-2229, 2002. https://doi.org/10.1109/TED.2002.805634

[15] T. Ernst, R. Ritzenthaler, O. Faynot, and S. Cristoloveanu, "A model of fringing fields in short-channel planar and triple-gate SOI MOSFETs," *IEEE transactions on electron devices,* vol. 54, no. 6, pp. 1366-1375, 2007. https://doi.org/10.1109/TED.2007.895241

[16] A. Aminbeidokhti, A. A. Orouji, S. Rahmaninezhad, and M. Ghasemian, "A novel high-breakdown-voltage SOI MESFET by modified charge distribution," *IEEE transactions on electron devices,* vol. 59, no. 5, pp. 1255-1262, 2012. https://doi.org/10.1109/TED.2012.2186580

[17] D. Madadi, A. A. Orouji, and A. Abbasi, "Improvement of nanoscale SOI MOSFET heating effects by vertical Gaussian drain-source doping region," *Silicon,* vol. 13, no. 3, pp. 645-651, 2021. https://doi.org/10.1007/s12633-020-00453-x

[18] M. G. C. de Andrade and J. A. Martino, "Threshold voltages of SOI MuGFETs," *Solid-State Electronics,* vol. 52, no. 12, pp. 1877-1883, 2008. https://doi.org/10.1016/j.sse.2008.06.046

Electrical Engineering Technical Journal, ISSN: ISSN: 3007-9772, Vol. 3, No. 1, 2026, Pages 8-13
DOI: https://doi.org/10.51173/eetj.v3i1.38

*Electrical Engineering Technical Journal*
Journal homepage: http://eetj.mtu.edu.iq

*RESEARCH ARTICLE*

# Development of a Software Application to Improve the Quality of a Visual Image

**Qossy Abbas Hameed [1], and Sviataslau Statkevich [1 *]**

[1] Department of Computer Engineering, Yanka Kupala State University of Grodno, Republic of Belarus

[*]Corresponding Author Email: sstat@grsu.by

**Article Info.**

Article history:

Received
2 October 2025

Accepted
15 November 2025

Published in Journal
7 December 2025

**Abstract**

A pixar image is not merely a visual representation of something; it carries within it a wealth of memories and important information. Image processing has been, and continues to be, a primary focus for many researchers seeking to improve image quality, given its importance in numerous vital areas of life that demand high precision for realistic assessment. Due to the heavy reliance on sensitive materials in many fields, and because of ambient noise, poor lighting, or compression distortion, image quality is compromised. This, in turn, limits the reliability of automated systems that depend on images for analysis and to provide dependable results. This paper aims to develop a Python-based program capable of increasing efficiency and improving the perceptual and analytical quality of digital images by applying and comparing different noise reduction and interpolation algorithms. Python was chosen for its high flexibility and open-source nature, allowing for the desired balance between computational efficiency and image clarity.

This is an open-access article under the CC BY 4.0 license (http://creativecommons.org/licenses/by/4.0/) Publisher: Middle Technical University

**Keywords**: Image Enhancement; Digital Filtering; Bicubic Interpolation; Gaussian Filter; PSNR Evaluation.

## 1. Introduction

Digital image processing remains a significant challenge due to its profound impact on computer vision systems and multimedia applications. This research, based on Python 3.9, focuses on enhancing digital image quality by integrating adaptive filtering and advanced interpolation algorithms. It combines established enhancement techniques, such as non-local mean filtering, Gaussian noise reduction, and two-cube interpolation, to improve contrast, sharpness, and overall quality. The combination of two-cube interpolation and non-local mean filtering demonstrates a significant advantage over traditional methods in terms of maximum signal-to-noise ratio (PSNR) efficiency and noise reduction. The proposed application achieved an 8%–12% increase in PSNR and an approximately 10% decrease in root mean square error (RMSE). It represents a practical, scalable, and cost-effective solution for improving image quality in medical, military, and security applications, as shown in Figure 1.

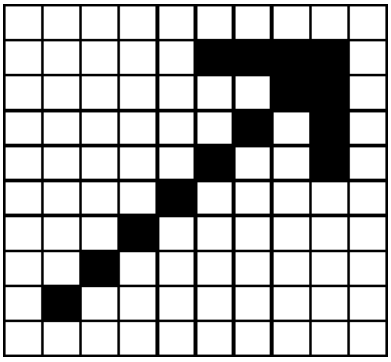

**Fig. 1.** Digital image processing engineering.

Previous studies in digital image enhancement explored a range of methods including linear filtering, wavelet-based denoising, and machine learning-driven super-resolution. Gonzalez and Woods established the theoretical basis of digital image enhancement [5], while Bovid expanded perceptual modeling for quality assessment [2]. More recent work by Tyagi introduced adaptive filtering models to optimize noise removal in dynamic environments as shown in Figure 2 [3]. Despite these advances, existing software often suffers from trade-offs between performance and computational cost. This gap motivated the current research to develop a lightweight, platform-independent Python application integrating high-performance enhancement algorithms [4].


**Fig. 2.** Comparison of existing image enhancement techniques.

## 2. Methods and Materials

The system was designed as a modular Python application using the OpenCV library. Programming and operating environment is Operating System Windows 11 Pro 64-bit (10.0, Build 22000) System Manufacturer: Dell c. System Model: Inspiron 5570 BIOS: 1.14.0 velour a Soft Processor: Intel(R) Core (TM) i5-8250U CPU@ 1.60GHz (8 CPUs), ~1.8GHz Memory: 16384MB RAM DirectX Version: DirectX 12. The enhancement process consists of three stages: preprocessing, filtering, and post-processing. The preprocessing phase includes image loading, format normalization, conversion to grayscale or color channels, and histogram analysis to detect underexposure or overexposure. These steps ensure consistent input for the enhancement algorithms as shown in Figure 3.

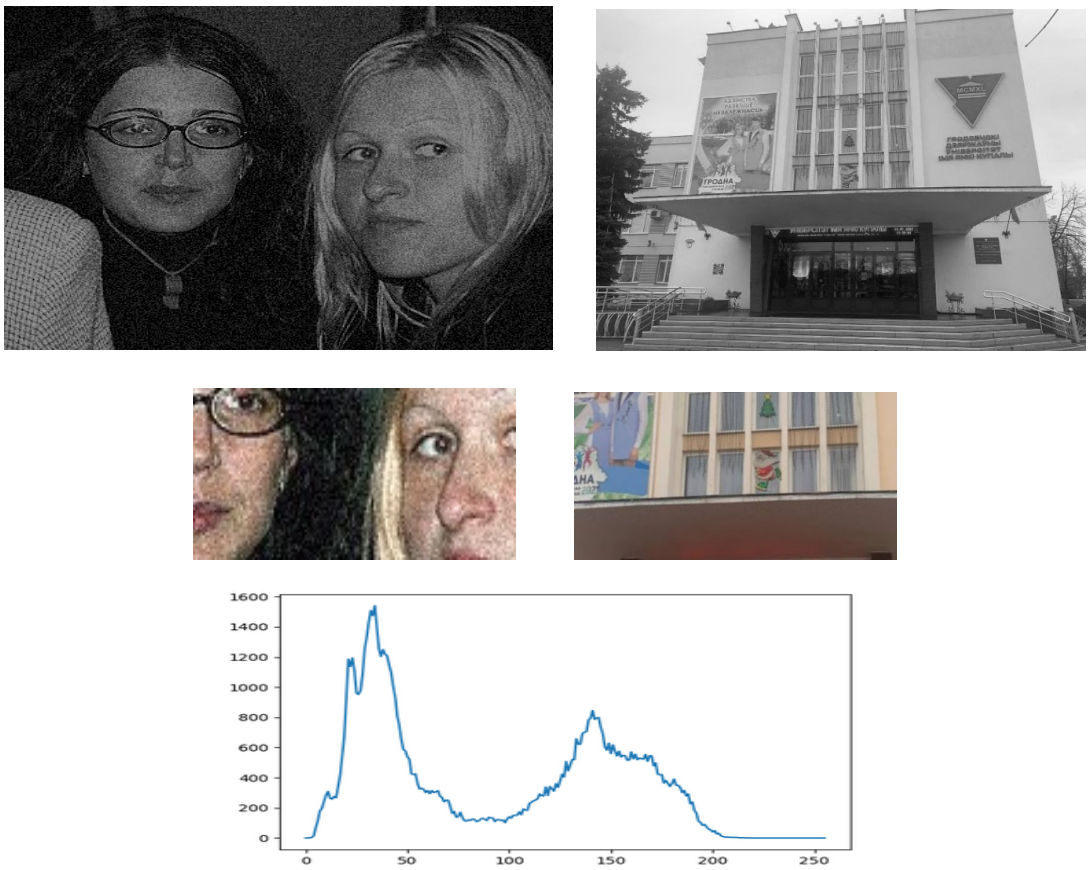


**Fig. 3.** Flowchart of preprocessing operations.

The enhancement module implements three major algorithms: non-local means filtering (NLM), Gaussian blur, and bicubic interpolation. NLM reduces random noise based on structural similarity rather than spatial proximity [6]. Gaussian blur smooths intensity variations by applying a weighted average across neighboring pixels [7]. Bicubic interpolation reconstructs missing data and provides sharper results than bilinear methods [8].

## 3. Evaluation Metrics

Image quality was evaluated using quantitative and qualitative metrics, including PSNR (Peak Signal-to-Noise Ratio), RMSE (Root Mean Square Error), and human visual inspection [9-13]. PSNR quantifies the difference between the enhanced and original images, while RMSE measures distortion magnitude as shown in Figure 4.

```
# checks the smoothness
S0 = np.ones((30, 30, 30)) * 100
S0[10:20, 10:20, 10:20] = 50
S0[20:30, 20:30, 20:30] = 0
S0_noise = S0 + 20 * np.random.standard_normal((30, 30, 30))
print("Original RMSE", np.sum(np.abs(S0 - S0_noise)) / np.sum(S0))

S0n1 = non_local_means(
    S0_noise,
    sigma=400,
    rician=False,
    patch_radius=1,
    block_radius=1)
print("Smaller patch RMSE", np.sum(np.abs(S0 - S0n1)) / np.sum(S0))
S0n2 = non_local_means(
    S0_noise,
    sigma=400,
    rician=False,
    patch_radius=2,
    block_radius=2)
print("Larger patch RMSE", np.sum(np.abs(S0 - S0n2)) / np.sum(S0))
S0n = adaptive_soft_matching(S0, S0n1, S0n2, 400)
print("ASCM RMSE", np.sum(np.abs(S0 - S0n)) / np.sum(S0))

assert_(np.sum(np.abs(S0 - S0n)) / np.sum(S0) <
        np.sum(np.abs(S0 - S0n1)) / np.sum(S0))
assert_(np.sum(np.abs(S0 - S0n)) / np.sum(S0) <
        np.sum(np.abs(S0 - S0_noise)) / np.sum(S0))
assert_(90 < np.mean(S0n) < 110)
```

**Fig. 4.** Interface of the developed Python application with image input and output panels.

(a) Before (b) After

**Fig. 5.** Result of applying PSNR.

- **RMSE (Root Mean Square Error)** measures overall distortion. This statistical measure is primarily used to evaluate the performance of prediction or regression models by measuring the average error between predicted and actual values. It has applications in many fields, including medicine, security, and surveillance. In medicine, RMSE is used to assess the accuracy of models in predicting continuous variables. In medical data analysis and imaging, it evaluates the accuracy of image reconstruction algorithms in medical imaging such as MRI and CT. It also assesses the accuracy of surgical measurements using robots; a lower RMSE value indicates less deviation from the intended movement or position, thus increasing the accuracy of the surgical procedure. In the fields of security and surveillance, RMSE is used to evaluate the accuracy of behavior or risk prediction models, or to assess the quality of sensing and detection systems. It measures the accuracy of models that predict security risks or threat levels in a given system, such as cybersecurity

systems or financial risk assessments for organizations. It also evaluates the performance of object tracking models in video surveillance systems. In security or environmental monitoring of large areas, it is used to assess the accuracy of digital elevation maps (DEM) collected by satellites or aerial surveys. RMSE is a crucial tool in the evaluation and monitoring phase of regression and prediction models within these applications, providing a direct numerical value that reflects the average error magnitude. The mean squared error (RMSE) is a powerful measure of the difference between an enhanced image and the original image. It is used because it has the same pixel count as the original image, making it more easily interpreted than the mean squared error (MSE). RMSE is calculated directly from MSE as follows: RMSE = $\sqrt{MSE}$. A lower RMSE value indicates better image restoration quality and greater distortion reduction [14].

- **Subjective visual inspection:** Human-perceived quality was also assessed. A proposed approach to integrating symbolic AI with deep learning involves designing hybrid models (neuro-symbolic AI) that utilize deep networks (such as CNNs or Transformers) to process raw data (images, text) and extract features. These features are then passed to symbolic logic algorithms to make inferences and decisions. The goal is to create AI systems capable of explaining their decisions using clear logical rules, rather than simply making predictions. Thus, medical diagnostic systems would not only provide a diagnosis but also a logical explanation based on established medical principles.
- **Statistical Validation:** To determine the superior performance of the non-local two-cubic average generation algorithm compared to traditional methods, a two-tailed t-test was performed. The test was conducted on the PSNR and RMSE values for all images in the dataset, at a significance level of $\alpha = 0.05$.
  Null hypothesis (H0): There is no statistically significant or exaggerated difference between the mean results of the proposed method and competing methods.
  Alternative hypothesis (Ha): There is a statistically significant difference.
  The results showed a p-value (probability value) less than 0.05 ($p<0.05$), indicating the rejection of the null hypothesis. This demonstrates that the performance improvement (increased PSNR and decreased RMSE) is statistically significant and reliable, enhancing the robustness and effectiveness of the developed application [14].

## 4. Estimating the Quality of the Decoded Image

One of the problems of computer graphics is that adequate criterion for assessing the loss of image quality has not yet been found. Quality is lost when digitizing, when converting to a limited palette of colors or into another color space, as well as when compressing images with losses [11].

Let there be two images: $f(x,y)$ – the original, and $f(x,y)$ – restored image of size $M \times N$. One of the simple criteria for assessing the loss of quality is the standard deviation of the pixel values of the compressed image from the original

$$d(x,y) = \sqrt{\frac{\sum_{x,y=1}^{M,N} \left( f(x,y) - f(x,y) \right)^2}{M \times N}} \quad (1)$$

According to this criterion, the image will be severely damaged when the brightness changes by only 5%. At the same time, an image with snow, a sharp change in the color of individual dots will be recognized as almost unchanged.
Another criterion is the maximum deviation from the original:

$$d(x,y) = \max_{x,y} \left| f(x,y) - f(x,y) \right| \quad (2)$$

This measure is extremely sensitive to the beating of individual pixels, i.e. only one pixel can change in the image, and this criterion recognizes the image as badly corrupted. In practice, a measure of image quality that is used is the signal-to-noise ratio (PSNR) criterion.

$$d(x,y) = 10 \cdot \lg \left( \frac{255^2 \cdot M \cdot N}{\sum_{x,y=1}^{M,N} \left( f(x,y) - f(x,y) \right)^2} \right) \quad (3)$$

This measure is similar to the standard deviation, but it is more convenient to use because of the logarithmic scale of the scale.
The loss in quality is best appreciated by the human eye. Image compression can be considered excellent if it is impossible to distinguish the original from the compressed image by eye. But in practice, with lossy compression, some distortion is always introduced into the image, noticeable when comparing the original and the compressed image.
To other most used quality assessment criteria an image include:

- average difference

$$AD = \frac{1}{MN} \sum_{x=1}^{M} \sum_{y=1}^{N} \left[ f(x,y) - f(x,y) \right] \quad (4)$$

- cross-correlation coefficient

$$K = \frac{\sum_{x=1}^{M} \sum_{y=1}^{N} f(x,y) \cdot f(x,y)}{\sum_{x=1}^{M} \sum_{y=1}^{N} \left[ f(x,y) \right]^2} \quad (5)$$

- image fidelity

$$\overline{AD} = 1 - \left( \frac{\sum_{x=1}^{M} \sum_{y=1}^{N} \left[ f(x,y) - f(x,y) \right]^2}{\sum_{x=1}^{M} \sum_{y=1}^{N} \left[ f(x,y) \right]^2} \right) \quad (6)$$

## 5. Results

Experiments were conducted using a dataset of 100 images with varying resolutions and noise levels. Comparative testing among the filtering techniques produced the following outcomes:

- Non-local means filtering achieved superior noise reduction with minimal edge blurring.
- Bicubic interpolation offered the best sharpness and detail reconstruction during resizing.
- Gaussian filtering improved smoothness but caused minor texture loss.

As shown in Figure 6, the visual comparison indicates that the bicubic–nonlocal combination increased PSNR by 8–12% and reduced RMSE by approximately 10% compared to conventional methods [10].

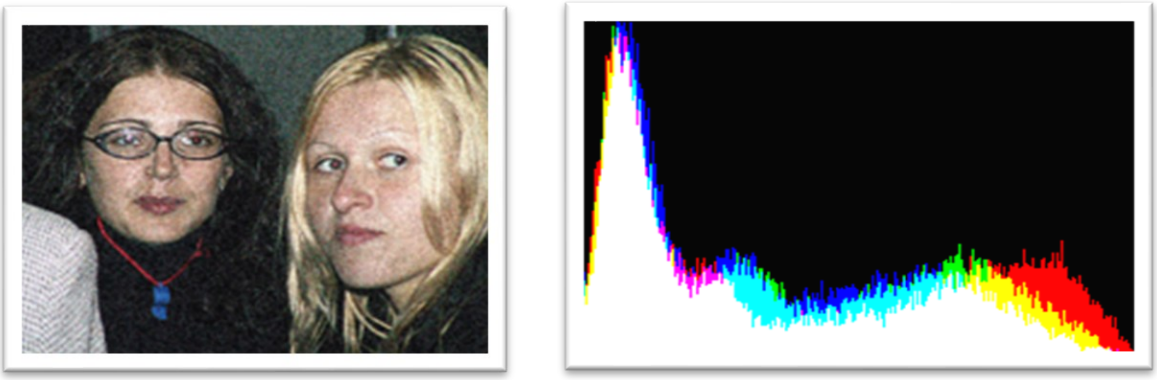

**Fig. 6.** Sample visual comparison between original, noisy, and enhanced images.

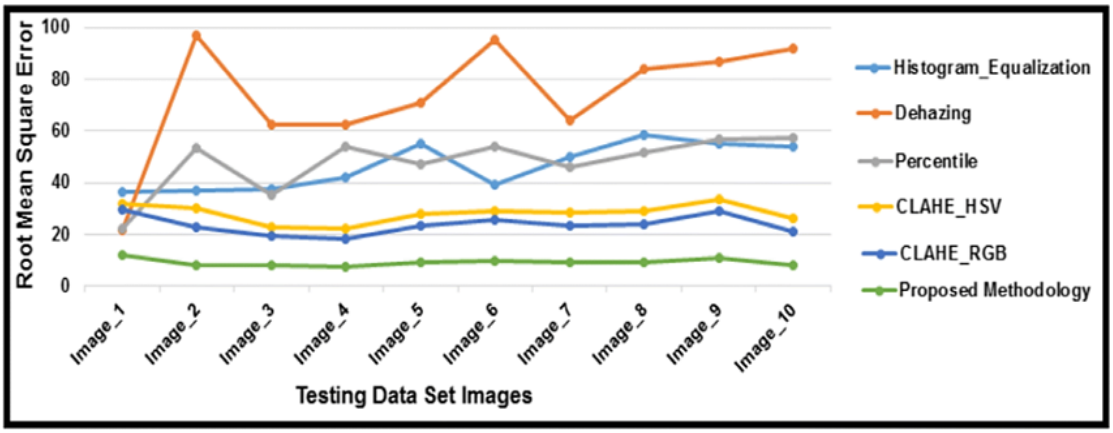


**Fig. 7**: Graph showing RMSE performance for different enhancement techniques.

Table 1 quantifies PSNR for filtering techniques between the enhanced and original image.

**TABLE 1.** PSNR for filtering techniques.

| NP% | CWM | MMEM | AFMF | MBD | WFM | HAF |
|---|---|---|---|---|---|---|
| 10 | 26.58 | 27.08 | 28.38 | 27.72 | 26.97 | 37.30 |
| 20 | 24.03 | 25.63 | 27.38 | 26.24 | 23.87 | 36.06 |
| 30 | 21.38 | 24.80 | 26.00 | 24.37 | 21.80 | 34.98 |
| 40 | 19.56 | 23.66 | 24.12 | 23.72 | 20.17 | 33.60 |
| 50 | 16.90 | 22.54 | 24.05 | 21.64 | 18.70 | 31.54 |

While these measures are effective in determining overall distortion, they do not necessarily reflect human-perceived quality completely. Although a subjective visual inspection was conducted, this evaluation was not documented using a standardized statistical methodology, leaving room for subjectivity in the qualitative assessment. The experiments were conducted on a relatively limited dataset. This limitation restricts the generalizability of the results to different data types (such as specialized medical images or high-resolution, high-speed surveillance footage) and diverse real-world noise environments. Although the non-local means (NLM) algorithm is superior in reducing noise, it is known for its high computational cost. Since the current system is based on a Python environment, achieving Real-Time Processing may face challenges, especially in applications that require high speed (such as security monitoring), which is our future proposal to integrate acceleration as the next step indicates.

## 6. Conclusion

This study presented the design and implementation of a Python-based software system for digital image quality enhancement. The integration of bicubic interpolation and non-local means filtering proved to be an effective approach to improving visual clarity and noise suppression. The developed tool offers a balance between processing speed and visual quality, platform independence and open-source accessibility, and potential applicability in surveillance, medical imaging, and visual inspection. Future work may involve integrating algorithms to improve training accuracy using deep learning methods with real-time GPU acceleration to enhance image reconstruction performance, in order to address several methodological and operational limitations associated with the proposed system when interpreting results and defining the scope of application. The quantitative evaluation of system performance relied primarily on two traditional measures: the maximum signal-to-noise ratio (PSNR) and the root mean square error (RMSE).

## References

[1] Pratt, W.K. Introduction to Digital Image Processing. CRC Press, 2014.DOI: 10.1201/b15731.
[2] Bovik, A. The Essential Guide to Image Processing. Academic Press, 2009.DOI: 10.1201/9780429451188.
[3] Tyagi, V. Understanding Digital Image Processing. Taylor & Francis Group, 2018.DOI: 10.1201/9781315123905.
[4] Anil, K.J. Fundamentals of Digital Image Processing. Prentice Hall, 1989.DOI : 10.1201/9781003221142 .
[5] Gonzalez, R.C. and Woods, R.E. Digital Image Processing. Prentice Hall, 2006.DOI: 10.1201/9781003221135.
[6] Szeliski, R. Computer Vision: Algorithms and Applications. Springer, 2011.DOI: 10.1201/9781003432036.
[7] David, J.P. and Forsyth, A. Computer Vision: A Modern Approach. Prentice Hall, 2011.DOI: 10.1201/9781003432036.
[8] Sandipan, D. Hands-On Image Processing with Python: Expert Techniques for Advanced Image Analysis. Packt Publishing, 2018. Doi 10.1201/9780429451188.
[9] Sugiyama, M. Introduction to Statistical Machine Learning. Morgan Kaufmann, 2015.DOI: 10.1201/b18188.
[10] Nirpjeet, E. A Review on Various Methods of Image Thresholding. International Journal on Computer Science and Engineering, 2011. ISSN: 0975-3397
[11] Dahlhaus, R. Mathematical Methods in Signal Processing and Digital Image Analysis. Springer, 2008. ISBN: 978-3-540-75632-3.
[12] Yuheng, S. and Hao, Y. Image Segmentation Algorithms Overview. Computer Science, 2017. DOI: 10.48550/arxiv.1707.02051
[13] Paulina Tsvetkova Department of Information Technologies, Bulgarian Academy of Sciences, University of Library Studies and Information Technologies Institute of Robotics, Sofia, Bulgaria; Georgi Dimitrov; Iva Kostadinova; Katia Rasheva-Yordanova; Lyubomir Gotsev; Pavel S. Petrov Image Processing Techniques In A Python Course Based on Ancient Manuscript Processing DOI**:** 10.1109/ACIT62333.2024.10712608
[14] Ullah, F., Kumar, K., Rahim, T. *et al.* A new hybrid image denoising algorithm using adaptive and modified decision-based filters for enhanced image quality. *Sci Rep* 15, 8971 (2025). DOI: 10.1038/s41598-025-92283-3

Electrical Engineering Technical Journal, ISSN: 3007-9772, Vol. 3, No. 1, 2026, Pages 14-19
DOI: https://doi.org/10.51173/eetj.v3i1.34

*Electrical Engineering Technical Journal*
Journal homepage: http://eetj.mtu.edu.iq

*RESEARCH ARTICLE*

# A Compact Tri-band Slotted Planar Inverted-F Antenna Design for 5G and WLAN Mobile Handsets

**Ashraf Sami Salman [1], Hussein Mohammed Naser [1], Faiz Arith [2]**

[1] Department of Computer Engineering, College of Engineering, Al-Naji University, Baghdad, Iraq
[2] Faculty of Electronic & Computer Engineering, University Technical Malaysia Melaka (UTeM), Durian Tunggal, Malaysia

* Corresponding author Email: ashraf.sami@alnaji-uni.edu.iq

**Article Info.**

Article history:

Received
22 September 2025

Accepted
5 November 2025

Published in Journal
2 January 2026

**Abstract**

This paper presents a compact, tri-band Planar Inverted-F Antenna (PIFA) for 5G sub-6 GHz mobile handsets. The proposed design integrates a slotted G-shaped radiating patch and a defected ground structure (DGS) to achieve multiband operation within a low-profile, four-layer printed structure. The antenna resonates at 2.4 GHz, 3.7 GHz, and 5.7 GHz, effectively covering the 5G NR bands n41 and n78, alongside LTE and WLAN applications. Simulation results demonstrate wide bandwidths of 770 MHz, 400 MHz, and 600 MHz at the respective resonant frequencies, with a peak realized gain of 4.4 dBi. The antenna exhibits high radiation efficiency, a low specific absorption rate (SAR), and an omnidirectional pattern. With its compact dimensions and performance metrics that surpass existing designs, the proposed antenna is a compelling solution for modern 5G-enabled mobile phones.

This is an open-access article under the CC BY 4.0 license (http://creativecommons.org/licenses/by/4.0/). Publisher: Middle Technical University

**Keywords**: 5G Antenna; DGS; PIFA; Sub-6 GHz; Tri-band.

## 1. Introduction

In recent years, there has been an increasing demand for mobile handsets that deliver higher data rates with enhanced reliability. This encompasses superior video calls, streaming high-definition content, and engaging in HD online gaming [1]. Thus, there is a critical need for fifth generation (5G) networks to exceed the capabilities of their predecessors. In contrast, as wireless devices become smaller, there is a need for multiband and compact antennas to reduce the number of antennas required in a limited space, thereby making room for other device components. Consequently, the planar inverted-F antenna (PIFA) is the recommended choice for mobile handsets' radio communications due to its small size, inexpensive manufacturing cost, compact structure, improved radiation features, high gain, and lower specific absorption rate (SAR). This quarter-wavelength patch antenna offers several features related to a half-wavelength patch antenna but is 50% smaller, making it optimal for mobile devices [2, 3]. However, a narrow bandwidth is a common limitation of PIFA. Numerous studies have focused on optimizing antenna configurations, some with multi-band resonance and others capable of wideband operation, often resulting in a trade-off between reduced gain, bandwidth, or design complexity.

A wideband antenna has been developed for LTE and WWAN applications in [4]. The antenna features a low profile and can demonstrate dual-resonant modes. However, it contains specific limitations, including its larger size, reduced gain, and limited bandwidth. A trapezoidal slotted PIFA with a rectangular patch has been developed in [5]. Despite its outstanding results and compact size, this antenna has a restricted bandwidth and requires enhancement to achieve a minimum return loss. As mentioned in [6], the designed wideband antenna includes a rectangular plate at the feeding pin with two cut slots to control high-frequency bands and a shorting pin for low-frequency bands. Although the antenna consists of a broad bandwidth, there is potential to enhance its average efficiency. Moreover, a multi-band antenna selectively covers the required band spectra [7], overcoming interference caused by a wideband antenna that covers unwanted spectra [8]. As mentioned in [9-13], switching diodes have been integrated into antennas to achieve frequency-reconfigurable responses, enhancing connectivity, adaptability to various frequency bands, and improving performance. However, this integration may add complexity to the design, require additional components, and increase manufacturing costs. In [14], researchers designed a dual-band frequency-tunable PIFA for handheld devices by varying the capacitance of the varactor diode. Despite this achievement's success, the design is complex and large, with limitations in bandwidth and gain.

This paper presents a low-profile tri-band PIFA designed for 5G mobile handsets within the sub-6 GHz communications spectrum. The radiating patch uses a G-shaped slot, mounted over two substrates to produce lower-frequency bands. Furthermore, the ground plane is carefully designed to facilitate operation in the higher-frequency band. The optimized PIFA resonates in the 2.4 GHz band (2.25–3.02 GHz), 3.7 GHz band (3.6–4 GHz), and 5.7 GHz band (5.5–6.1 GHz) to cover 5G NR (n41, n78), LTE, and WLAN bands. The suggested PIFA has been designed and simulated using CST simulation software. To validate the antenna results, the HFSS simulation software has been employed in the suggested design, and the results have been compared. The results indicate that the proposed PIFA is suitable for handheld devices in 5G due to its small size and its features of operating on three sub-6 GHz bands, which is considered an important characteristic to minimize the number of antennas used in wireless devices.

## 2. Design Method of Proposed PIFA

The proposed design, illustrated in Figure 1, consists of four distinct layers. Figure 1(a) shows the initial layer as a slotted, flipped G-shaped rectangular patch measuring 22 × 20 mm². The second layer comprises a low-cost FR4 substrate, characterized by a relative permittivity of 4.3 and a thickness of 0.8 mm. Figure 1(b) illustrates the subsequent layer, a vacuum layer consisting of an air gap with a dielectric constant of 1 and a height of 3 mm, which enhances bandwidth in the suggested design. The fourth and final layer is a ground plane shown in Figure 1(c) with dimensions of 39 × 20 mm². The feeding technique employed is coaxial feeding, which contributes to bandwidth optimization. Experiments have shown that the location of feeding significantly impacts overall antenna performance. Consequently, the feeding location has been optimized, as illustrated in Figure 1(c), to achieve the best results. Additionally, the multiple openings in the design enhance the vibration state, greatly increasing the amplitude of the electromagnetic waves. The overall dimensions of the proposed design are 39 × 20 × 3.8 mm³. Table 1 shows the dimensions of the proposed design.

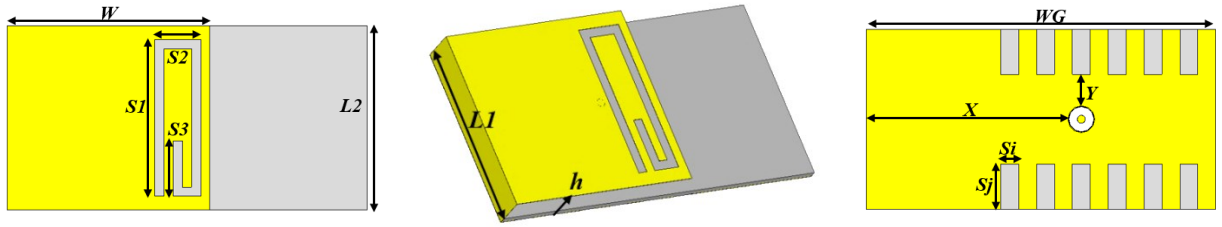


(a) (b) (c)

**Fig. 1.** Geometric shape of the proposed PIFA. (a) Front View, (b) Back View, (c) 3D View.

**TABLE 1.** Dimensions of the proposed PIFA design.

| Parameters | Value (mm) |
|---|---|
| W | 22 |
| WG | 39 |
| L1 | 20 |
| L2 | 20 |
| X | 22 |
| Y | 4 |
| S1 | 17 |
| S2 | 5 |
| S3 | 6 |
| Si | 2 |
| Sj | 5 |
| h | 3.8 |

The following formula is applied in the suggested PIFA design, with resonating frequencies improved through the use of a slotted radiating patch and defected ground structure (DGS). Figure 1 exhibits the dimensions used in the formula [16]:

$$f_0 = \frac{c}{4(L2+W-L1-h)\sqrt{\varepsilon_r}} \quad (1)$$

Where c is the free-space speed of light, and $\varepsilon r$ is the dielectric constant of the substrate.

The shorting pin or plate plays a crucial role in reducing the size of the PIFA and can be calculated using the following formulas [2, 17]:

Case 1

$If\ L1=L2\ ;\ W=\lambda/4$

Case 2

$If\ L1\approx 0\ ;\ W+L2=\lambda/4$

The proposed antenna design is specifically intended for a frequency of 3.7 GHz. Considering this antenna is designed for mobile handsets, reducing the number of antennas is crucial to make room for other electronic components. Therefore, the design has been modified to enable tri-band resonance. To allow the antenna to resonate in dual-band mode, the radiating patch has been slotted with a flipped G-shape. This causes the antenna to resonate at 2.4 and 3.7 GHz, as shown in Figure 2. The ground structure has been divided into six small symmetrical rectangles, enabling the antenna to resonate in a tri-band mode and providing an omnidirectional radiation pattern. In addition, using a rectangular DGS optimizes the antenna bandwidth [18]. The shorting plate has been incorporated instead of the shorting pin between the radiating patch and ground plane to achieve maximum radiation efficiency while maintaining the desired resonant frequency.

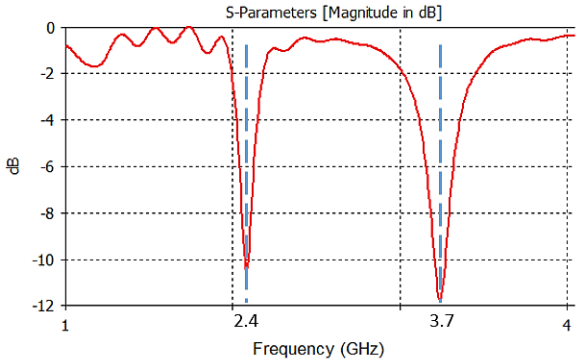


**Fig. 2.** Dual-band mode with slotted radiator.

## 3. Simulation Results and Analysis

This section presents and discusses the results of the suggested design, including return loss, VSWR, radiation pattern, SAR, and efficiency. The antenna under consideration exhibits resonance at frequencies of 2.4 GHz, 3.7 GHz, and 5.7 GHz, with corresponding impedance bandwidths of 779 MHz, 400 MHz, and 600 MHz. This configuration effectively covers the 5G NR bands n41 (2496–2690 MHz), n78 (3300–3800 MHz), and WLAN applications. Figure 3 compares the simulated antenna in CST and HFSS. The impedance bandwidth threshold is lower than -10 dB.

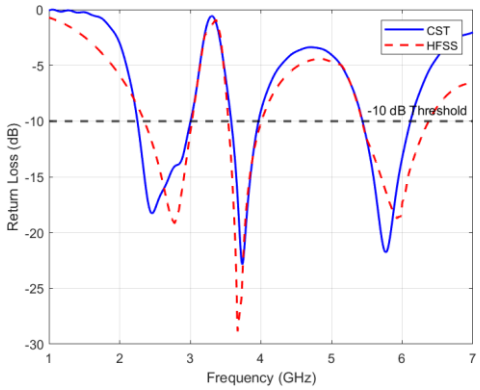


**Fig. 3.** The proposed tri-band PIFA return loss behavior versus frequency.

Figure 4 illustrates the impedance matching of the suggested antenna, as indicated by the VSWR at the resonance frequencies. In general, the antenna VSWR is 2:1, indicating that the transmitter directs the energy towards the antenna. The comparison ratio reveals an optimal match of less than two, while the frequency of 5.7 GHz yields approximate results.

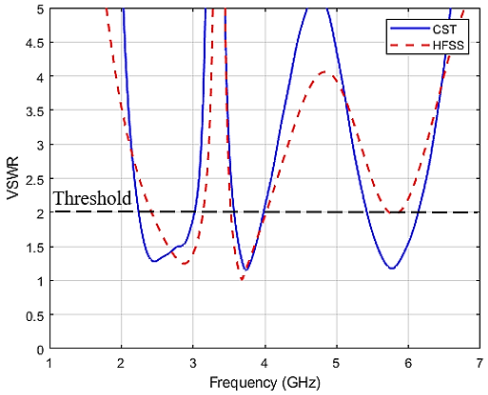


**Fig. 4.** VSWR as a function of frequency.

The proposed antenna radiates omnidirectionally at its resonant frequencies. Figure 5 presents a 3D radiation pattern exhibiting realized gains of 2.7 dB, 3.5 dB, and 4.4 dB, respectively. The gain increases with frequency. The reduced antenna size and the use of FR4 material decrease the antenna's gain. However, using different semiconductor materials can further affect the outputs [19].

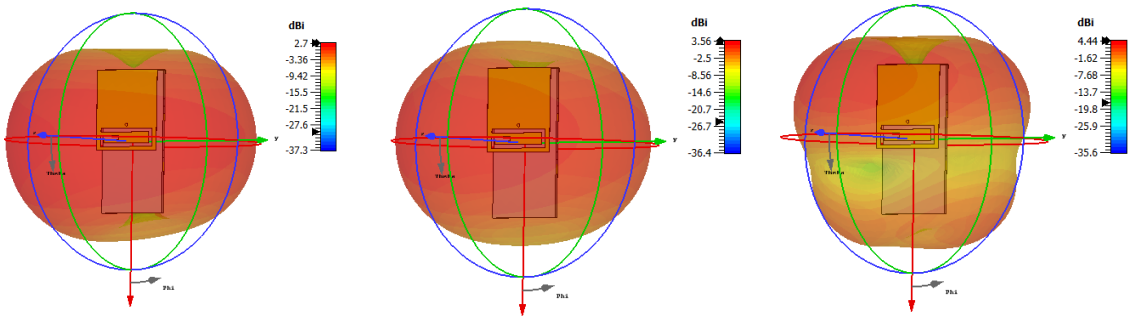


(a) (b) (c)

**Fig. 5.** Realized gain in the 3D radiation pattern of the suggested tri-band PIFA.

As illustrated in Figure 6, the proposed antenna highlights the key parameters and their relationship, with the antenna efficiency measured by the following formula:

$$\eta = \frac{G}{D} \tag{2}$$

The suggested PIFA demonstrates a high efficiency of 98% at frequencies 2.4 GHz and 3.7 GHz, while at 5.7 GHz, the efficiency reaches 96%.

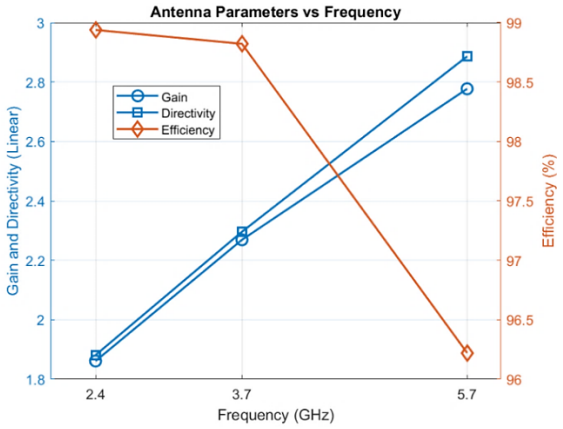


**Fig. 6.** Antenna parameters at operating frequencies.

This type of antenna is known for its low SAR on human tissues, lower head loss [20], and compact size. In Europe, the SAR limit for the head is 2 W/kg, averaged over a volume of 10 grams of tissues [21]. Figure 7 shows that the SAR calculations indicate that the proposed antenna has an acceptable and low effect on human head tissues. The simulated results are 0.77, 0.99, and 0.84 W/kg at resonance frequencies, when a distance of 2 mm from the head is considered.

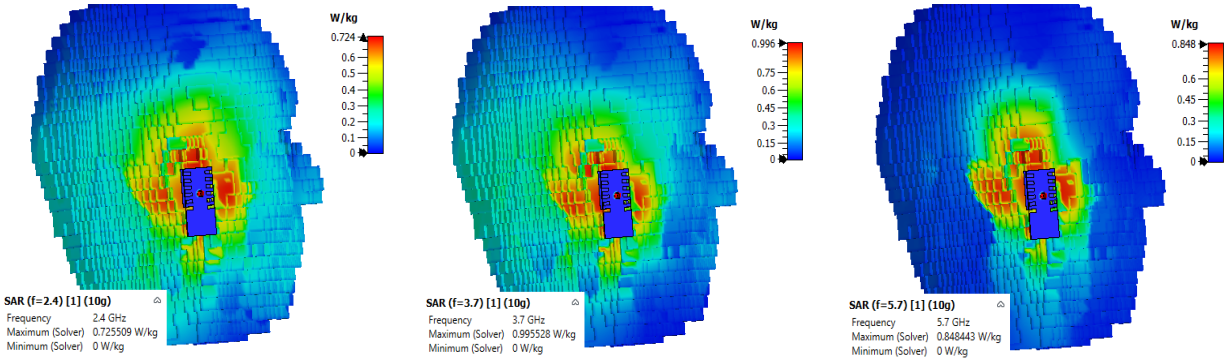


(a) (b) (c)

**Fig. 7.** Proposed PIFA SAR on human head tissues.

The CST simulation software has been utilized to design and showcase the proposed antenna's results, while the HFSS simulation software has been employed to validate these outcomes. The proposed antenna is promising in 5G networks for mobile handsets due to its compact design and the results obtained in comparison to earlier research. Table 2 presents a comparison of the proposed design's results with results from prior studies. The proposed antenna demonstrates high efficiency, functions at three resonance frequencies, offers a broad bandwidth, and maintains a compact design.

**TABLE 2.** Proposed PIFA evaluation with earlier investigations.

| Ref. | Dimensions (mm) | Operating Bands (GHz) | Bandwidth (GHz) | Gain (dBi) | Efficiency (%) |
|---|---|---|---|---|---|
| [7] | 20 × 16 × 1.6 | 2.45 | 2.38–2.51 | 2 | 86 |
| | | 3.5 | 3.44–3.84 | 2.1 | 86 |
| | | 5.8 | 5.53–7.23 | 2.5 | 86 |
| [22] | 110 × 110 × 23 | 2.59 | 2.51–2.68 | 7.6 | 82 |
| | | 3.5 | 2.51–2.68 | 8.5 | 81 |
| | | 4.9 | 4.73–5 | 12.1 | 89 |
| [23] | 38 × 40 × 1.9 | 1.32 | 1.28-1.38 | 2.5 | 96 |
| | | 3.12 | 3.05-3.17 | 4.5 | 90 |
| | | 5.2 | 4.93-5.44 | 6 | 95 |
| [24] | 15 × 20 | 2.45 | 2.35–2.5 | 1.84 | 75 |
| | | 3.5 | 3.3–3.55 | 2.13 | 75 |
| | | 5.8 | 5.18–7.63 | 2.72 | 75 |
| [25] | 60 × 50 × 1.6 | 1.8 | 1.4-2 | 2.34 | 73 |
| | | 3.5 | 3.4-3.8 | 5.2 | 68 |
| | | 5.4 | 5.2-5.6 | 1.42 | 59 |
| This Work | 39 × 20 × 3.8 | 2.4 | 2.25 - 3.02 | 2.7 | 98 |
| | | 3.7 | 3.6 - 4 | 3.56 | 98 |
| | | 5.7 | 5.5 – 6.1 | 4.44 | 96 |

## 4. Conclusion

This study presents a compact tri-band PIFA suitable for sub-6 GHz 5G mobile handsets. The proposed design achieves a small form factor through the use of a shorting plate while maintaining high radiation efficiency. Furthermore, the incorporation of a DGS enables an omnidirectional radiation pattern and tri-resonant operation. The antenna effectively covers the essential 5G NR, LTE, and WLAN bands. When measured by the bandwidth of the impedance, it operates at different frequencies for the given ranges, with different gains as well. Simulations performed with both CST and HFSS show good agreement in performance, with only minor discrepancies in the VSWR at the 5.7 GHz band. The antenna also demonstrates compliance with safety standards for portable devices through its low SAR values. In comparison to existing designs, this antenna offers a compelling combination of enhanced bandwidth, high efficiency, and a compact footprint. These attributes position it as a highly suitable candidate for integration into future 5G mobile handsets. The future work will address the use of FR-4 and Rogers materials for their cost and efficiency benefits in the proposed antenna, including model fabrication and comparison of measurement results with simulations.

## References


[1] R. Hussain, A. T. Alreshaid, S. K. Podilchak, and M. S. Sharawi, "Compact 4G MIMO antenna integrated with a 5G array for current and future mobile handsets," IET microwaves, antennas & propagation, vol. 11, no. 2, pp. 271-279, 2017, doi: /10.1049/iet-map.2016.0738.

[2] K. Kundu, A. Dubey, A. Dhama, and N. N. Pathak, "Planar inverted F antenna, PIFA array in 5G applications," in Journal of Physics: Conference Series, 2021, vol. 2062, no. 1: IOP Publishing, p. 012002, doi: /10.1088/1742-6596/2062/1/012002.

[3] Y. Xu and H. M. Zhou, "Small-size narrow-frame PIFA for LTE/WWAN/GNSS handset application," Microwave and Optical Technology Letters, vol. 58, no. 7, pp. 1689-1693, 2016, doi: /10.1002/mop.29891.

[4] A. Affandi, R. Azim, M. M. Alam, and M. T. Islam, "A low-profile wideband antenna for WWAN/LTE applications," Electronics, vol. 9, no. 3, p. 393, 2020, doi: /10.3390/electronics9030393.

[5] P. Sharma and P. P. Bhattacharya, "A Novel Planar Inverted-F Antenna for Dual Band Operations," in 2020 International Conference on Emerging Trends in Communication, Control and Computing (ICONC3), 2020: IEEE, pp. 1-4, doi: /10.1109/ICONC345789.2020.9117276.

[6] A. Yacoub, M. Khalifa, and D. N. Aloi, "Wide bandwidth low profile PIFA antenna for vehicular sub-6 GHz 5G and V2X wireless systems," Progress In Electromagnetics Research C, vol. 109, pp. 257-273, 2021, doi: /10.2528/PIERC21010609.

[7] A. U. Fakhriddinovich, M. A. Sufian, W. A. Awan, N. Hussain, and N. Kim, "A Compact Antenna With Multiple Stubs for ISM, 5G Sub-6-GHz, and WLAN," IEEE Access, vol. 11, pp. 130418-130425, 2023, doi: 10.1109/access.2023.3333881.

[8] M. M. Alam, R. Azim, N. M. Sobahi, A. I. Khan, and M. T. Islam, "A dual-band CPW-fed miniature planar antenna for S-, C-, WiMAX, WLAN, UWB, and X-band applications," Scientific Reports, vol. 12, no. 1, p. 7584, 2022, doi: /10.1038/s41598-022-11679-7.

[9] F. A. Asadallah, J. Costantine, and Y. Tawk, "A multiband compact reconfigurable PIFA based on nested slots," IEEE antennas and wireless propagation letters, vol. 17, no. 2, pp. 331-334, 2018, doi: /10.1109/LAWP.2017.2788465.

[10] A. Ghaffar et al., "A Frequency Reconfigurable Compact Planar Inverted-F Antenna for Portable Devices," International Journal of Antennas and Propagation, vol. 2022, pp. 1-9, 2022, doi: 10.1155/2022/7239608.

[11] A. Ghaffar et al., "Design and realization of a frequency reconfigurable multimode antenna for ISM, 5G-sub-6-GHz, and S-band applications," Applied Sciences, vol. 11, no. 4, p. 1635, 2021, doi: /10.3390/app11041635.

[12] G. Jin, C. Deng, Y. Xu, J. Yang, and S. Liao, "Differential Frequency-Reconfigurable Antenna Based on Dipoles for Sub-6 GHz 5G and WLAN Applications," IEEE Antennas and Wireless Propagation Letters, vol. 19, no. 3, pp. 472-476, 2020, doi: 10.1109/lawp.2020.2966861.

[13] J. Zhang, S. Yan, and G. A. Vandenbosch, "Metamaterial-inspired dual-band frequency-reconfigurable antenna with pattern diversity," Electronics Letters, vol. 55, no. 10, pp. 573-574, 2019, doi: /10.1049/el.2019.0329.

[14] S. Ganesh and Y. K. Choukiker, "Dual band frequency tunable planar inverted-F antenna for mobile handheld devices," International Journal of RF and Microwave Computer-Aided Engineering, vol. 30, no. 5, 2020, doi: 10.1002/mmce.22150.

[15] A. A. Deshmukh, T. P. Page, and V. A. Chavali, "Dual Band Circular Polarized Design of Rectangular Microstrip Antenna For GPS L-band and Galileo E-band Applications," Indonesian Journal of Electrical Engineering and Informatics (IJEEI), vol. 13, no. 1, pp. 261-276, 2025, doi: doi: 10.52549/ijeei.v13i1.5211.

[16] C. A. Balanis, "Antenna theory: analysis and design," vol. 4, Microstrip and Mobile Communications Antennas: John wiley & sons, 2016, pp. 783-867.

[17] E. Palantei, R. S. Madika, M. Baharuddin, and S. Syarif, "Design of Reconfigurable Planar Inverted F Antenna for 5G Implementation," in 2019 IEEE International Conference on Communication, Networks and Satellite (Comnetsat), 2019: IEEE, pp. 41-46, doi: /10.1109/COMNETSAT.2019.8844073.

[18] A. Boutejdar and W. Abd Ellatif, "A novel compact UWB monopole antenna with enhanced bandwidth using triangular defected microstrip structure and stepped cut technique," Microwave and Optical Technology Letters, vol. 58, no. 6, pp. 1514-1519, 2016, doi: doi.org/10.1002/mop.29820.

[19] I. Amiri and A. N. Z. Rashed, "Power enhancement of the U-shape cavity microring resonator through gap and material characterizations," Journal of Optical Communications, vol. 45, no. s1, pp. s63-s67, 2025, doi: doi.org/10.1515/joc-2019-0108.

[20] K. R. Boyle, M. Udink, A. de Graauw, and L. P. Ligthart, "A dual-fed, self-diplexing PIFA and RF front-end," IEEE transactions on antennas and propagation, vol. 55, no. 2, pp. 373-382, 2007, doi: doi.org/10.1109/TAP.2006.889852.

[21] D. Tan, "Modeling the specific absorption rate distribution of a smartphone," ANSYS Inc.: Canonsburg, PA, USA, 2012. [Online]. Available:https://s3-ap-southeast-2.amazonaws.com/public-leapaust/resources/Modeling+the+Specific+Absorption+Rate+Distribution+of+a+Smartphone+-+Application+Brief.pdf .

[22] Z. Duan, S. Shen, and G. Wen, "A Compact Tri-Band Filtering Antenna System for 5G Sub-6 GHz Applications," IEEE Transactions on Antennas and Propagation, vol. 70, no. 11, pp. 11097-11102, 2022, doi: 10.1109/tap.2022.3188346.

[23] L. Wakrim, A. Khabba, J. Amadid, and S. Ibnyaich, "A Semi-Defected Ground Plane and a Binary Genetic Algorithm for Designing a Very Compact Triple-Band Pifa Antenna," Jordanian Journal of Computers and Information Technology, no. 0, 2022, doi: 10.5455/jjcit.71-1652950714.

[24] W. A. Awan, N. Hussain, J. Lee, Q. Hussain, M. A. Sufian, and N. Kim, "Stub loaded Compact Size Tri-Band Antenna for ISM, 5G sub-6-GHz, IoT Applications," in 2022 Asia-Pacific Microwave Conference (APMC), 2022: IEEE, pp. 539-541, doi: /10.23919/APMC55665.2022.9999876.

[25] A. S. Elkorany et al., "Implementation of a Miniaturized Planar Tri-Band Microstrip Patch Antenna for Wireless Sensors in Mobile Applications," Sensors (Basel), vol. 22, no. 2, Jan 16 2022, doi: 10.3390/s22020667.

Electrical Engineering Technical Journal, ISSN: ISSN: 3007-9772, Vol. 3, No. 1, 2026, Pages 20-27
DOI: https://doi.org/10.51173/10.51173/eetj.v3i1.46

*Electrical Engineering Technical Journal*
Journal homepage: http://eetj.mtu.edu.iq

*RESEARCH ARTICLE*

# Tracking the Path of a Mobile Robot Using Fuzzy Logic Algorithms

**Huda Ali Muhammad [1], and Khosro Khandani [1 *]**

[1] Electrical Engineering Department of Mechatronics, Arak University, Iran

[*]Corresponding Author Email: k-khandani@araku.ac.ir

**Article Info.**

Article history:

Received
02 January 2026

Accepted
26 January 2026

Published in Journal
31 January 2026

**Abstract**

This paper presents a structured hybrid control framework for mobile robot navigation and path tracking in uncertain and dynamic environments. The proposed architecture integrates a fuzzy logic controller as the primary decision-making layer with a multilayer perception (MLP) neural network used for nonlinear compensation. The fuzzy module processes real-time sensory inputs from front, left, and right distance measurements and generates the initial steering command using a Mamdani inference system. To enhance tracking accuracy and robustness, the neural network is trained in a supervised manner using the mean squared error (MSE) loss function to learn adaptive correction signals. The final steering command is obtained by combining the fuzzy output with the neural compensation term, forming a hybrid control strategy that preserves interpretability while improving adaptability. The system is implemented in a simulation environment and evaluated under obstacle-rich scenarios. Quantitative performance metrics, including MSE and root mean square error (RMSE), are used to assess tracking accuracy. Experimental results demonstrate improved trajectory precision, reduced tracking error, and enhanced stability compared to standalone fuzzy and neural approaches. The proposed framework maintains clear functional separation between decision-making and compensation layers, improving modularity, transparency, and reproducibility. The results confirm that the integration of fuzzy reasoning with neural compensation provides an effective and computationally efficient solution for autonomous mobile robot navigation in nonlinear and uncertain environments.

This is an open-access article under the CC BY 4.0 license (http://creativecommons.org/licenses/by/4.0/) Publisher: Middle Technical University

**Keywords**: Mobile Robot; Fuzzy Logic; Path Tracking; Intelligent Control; Autonomous Navigation.

## 1. Introduction

Intelligent robots are designed to perform autonomous tasks without direct human intervention. Remote control systems enable human–robot interaction without physical presence, offering flexibility in hazardous or inaccessible environments. Efficient navigation algorithms that allow coordinated movement and collision avoidance are key challenges in autonomous robotics [1, 2].

Artificial neural networks (ANNs) replicate human brain learning and decision-making processes. Composed of interconnected neurons, neural networks can retain sensory information and learn via repetition [3, 4]. Neural networks also foster interdisciplinary collaboration across computer science, engineering, and neuroscience, accelerating advancements in practical applications [2, 5].

Robotic systems face challenges in dynamics and inverse dynamics, requiring advanced software to handle complex nonlinear equations [6]. Increased paths and obstacles heighten complexity, leading to trajectory deviations due to environmental uncertainties. Adaptive control techniques, particularly computed torque methods, help mitigate these effects but face limitations in nonlinear and rapidly changing conditions [7, 8]. Linking Python and MATLAB applications is essential to optimize simulation outcomes. Ordered neural network models support efficient, collision-free path planning while accommodating variable obstacle shapes [9, 10].

There is no meaningful correlation between the Vector Field Histogram (VFH) method and ultrasonic sensor-based path detection in mobile robots [11, 12]. This lack of relationship poses challenges for autonomous navigation, particularly in hazardous industrial or military applications. The primary objective of this research is to develop a robotic simulator leveraging neural networks to improve tracking performance of manipulators with unknown dynamics [5, 7]. The system integrates VFH and complementary algorithms to generate appropriate torque signals for precise trajectory following [2, 6].

The study is structured to progress logically from introduction to methodology, simulation, results, discussion, and conclusion, ensuring clarity and coherence in presenting contributions to autonomous robotics [9, 13].

## 2. Literature Review

Neural networks are widely used to model nonlinear robotic systems by processing inputs through weighted connections, biases, and activation functions [3, 4], with applications including inverse kinematics, dynamic control, and trajectory optimization [6, 7]. Hybrid neuro-fuzzy approaches further improve system adaptability under uncertainty and environmental variation [14, 15], while robots also employ computer vision and neural networks to construct internal representations of their environments for obstacle avoidance and path planning [9, 10]. In social and collaborative contexts, AI systems recognize human behaviors and intentions, enhancing operational safety and compliance [2, 5]. Motion planning defines sequences of movements that allow robots to reach target positions while avoiding obstacles [2, 13], utilizing common algorithmic categories such as path-based algorithms like A* and Dijkstra [1] and behavior-based models that predict motion using dynamic constraints [6]. Key challenges include large data volume, dynamic environments, and real-time execution

requirements [9, 10], though these algorithms are applied extensively in industrial robotics, autonomous vehicles, and gaming systems [11, 12].

The Vector Field Histogram (VFH) method enables real-time obstacle avoidance by representing obstacle density in polar histograms [11, 12], while Radial Basis Function Networks (RBFNs) enhance prediction and classification tasks due to their fast learning and approximation capabilities [3, 5]. Embedded robotic systems rely on neural networks to process internal sensors (e.g., encoders) and external sensors (ultrasonic, infrared, laser) for localization and navigation [7, 9], often using multilayer neural networks to compensate for sensor noise and cumulative errors to improve environmental map accuracy [3, 5]. Recent studies demonstrate that hybrid approaches combining neural networks, fuzzy logic, and visual servoing (IBVS/PBVS) significantly improve real-time path tracking and collision avoidance [14, 15]. Finally, experimental evaluations confirm enhanced trajectory accuracy and robustness in dynamic environments [16].

## 3. Practical Application

In this section, the simulation process was applied practically by connecting the neural network to the artificial intelligence camera to recognize the movement of the robot along the specified paths, as shown in Figure 1.

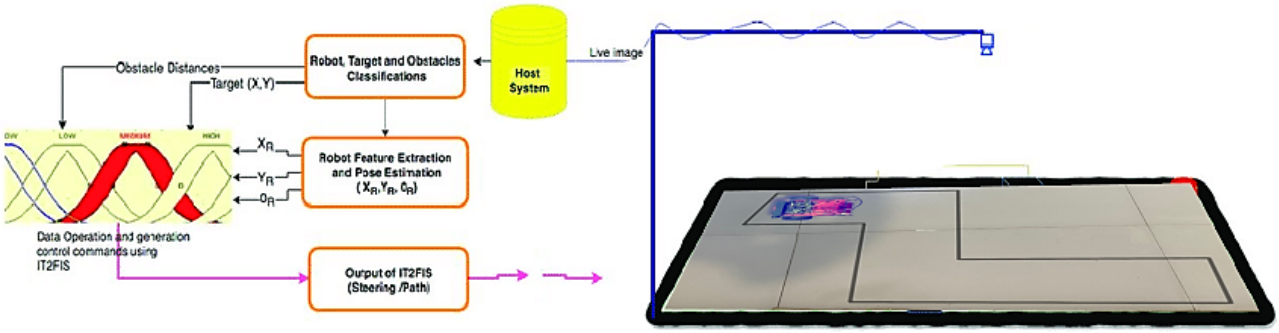


**Fig. 1.** Determining the path and direction of the robot using the camera.

Figure 1 shows the process of determining the direction and touch of the robot through a camera connected via a Wi-Fi network to the robot, where the data is sent through the pre-implemented simulation system, which determines the correct path to reach the goal [19]. In this study, various methods of route planning and obstacle avoidance of mobile robots are studied. Using these algorithms, a possible path is determined between the starting points and the target in such a way that no collision occurs between the robot and the obstacles, as shown in Figure 2.

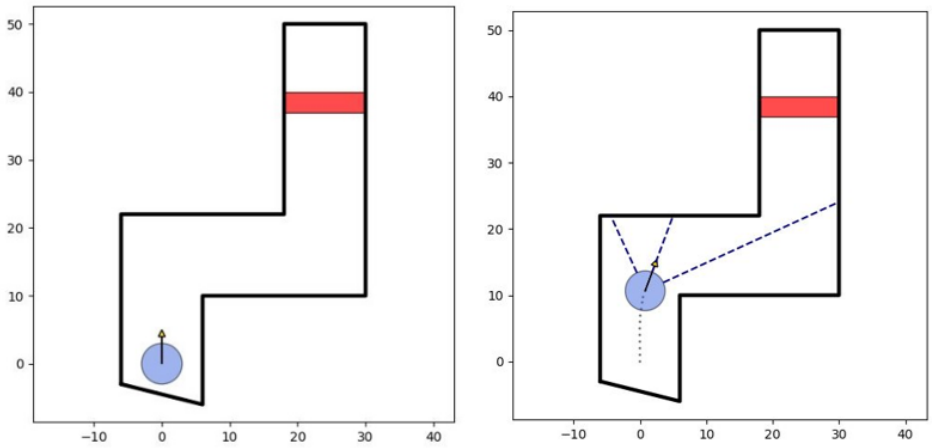

**Fig. 2.** The mechanism of the robot's movement and how it collides with obstacles during training.

Also, the study that was conducted in the proposed message is considered the best and most important in terms of simulation and design, through which the movement process is carried out in a simulated manner of a real robot movement in terms of design and the proposed environment, as shown in the following figure of the proposed results. Figure 3 demonstrates the mechanism followed by the distance sensor placed in the robot, which can determine whether there is an obstacle or not.

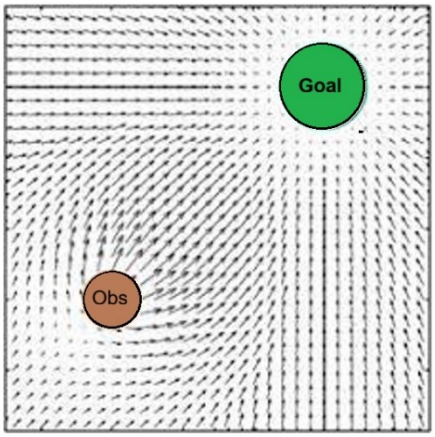


**Fig. 3.** Operational mechanism of the robot's distance sensor for obstacle detection and environment mapping.

The robot's movement from the starting point to the target point, comparing the time it takes to reach the target, is shown in Table 1. The first column shows the time it takes for the system to move without activating the neural network training, while the second column indicates the time the robot takes to reach the target. Here, it demonstrates the use of the neural network with the system for training the robot to reach the target in the shortest possible time.

**TABLE 1.** Comparative analysis of execution times required to reach the target position.

| cases | Time with Training ms | Time Outside of Training ms |
|---|---|---|
| **case01** | 5.12 | 3.70 |
| **case02** | 10.45 | 7.33 |
| **case03** | 11.87 | 12.17 |
| **case04** | 47.33 | 60.77 |
| **case05** | 31.44 | 20.34 |
| **case06** | 17.85 | 8.96 |
| **case07** | 16.74 | 12.57 |
| **case08** | 6.22 | 6.82 |
| **case09** | 5.80 | 3.69 |

The kinematic model of the mobile robot is described using discrete-time equations that define the evolution of the robot's position and orientation as follows:

$$x(t+1) = x(t) + cos[\emptyset(t) + \theta(t)] + sin[\theta(t)]\, sin[\emptyset(t)] \quad (1)$$

$$y(t+1) = y(t) + sin[\emptyset(t) + \theta(t)] - sin[\theta(t)]\, cos[\emptyset(t)] \quad (2)$$

$$\emptyset(t+1) = \emptyset(t) - arc\, sin[\tfrac{2\, sin[\theta(t)]}{b}] \quad (3)$$

where $x(t)$ and $y(t)$ represent the Cartesian position of the robot, $\phi(t)$ denotes its orientation, $\theta(t)$ is the steering control input, and b represents the distance between the robot wheels. These equations capture the nonlinear behavior of the mobile robot system. As a result, conventional control techniques exhibit limited performance in dynamic and uncertain environments, motivating the use of intelligent control strategies such as neural networks and fuzzy logic controllers [20- 22].

## 4. Implementation and Results

*4.1. Role of the Neural Network Controller*

The neural network controller is employed to approximate system nonlinearities and uncertainties present in the kinematic and dynamic models. The neural network estimates:

- External disturbances acting on the system
- Unmodeled dynamics
- Unknown or time-varying system parameters

The output of the neural network is then used to compensate for these nonlinearities within the control law, thereby improving trajectory tracking accuracy and system robustness [23].

*4.2. Role of the Fuzzy Logic Controller*

The fuzzy logic controller (FLC) relies on linguistic rules to handle uncertainty in sensor measurements, particularly in environments with dynamic obstacles. Typical fuzzy rules are defined as:

**IF** distance is *Near* **AND** angle is *Large*

**THEN** steering angle is *High*

This rule-based approach enables flexible decision-making without requiring an exact mathematical model of the environment. The fuzzy controller generates the steering angle $\theta(t)\backslash\text{theta(t)}\theta(t)$ required for obstacle avoidance while maintaining motion stability [22].

*4.3. Hybrid Neural–Fuzzy Controller*

The neural network and fuzzy logic controller are integrated within a hybrid control framework defined as:

$$\emptyset(t)f(x) = \frac{\sum_{i=1}^{n} \mu i(e,\dot{e}).yi}{\sum_{i=1}^{n} \mu i(e,\dot{e})} + \sum_{i=1}^{n} \omega j \emptyset j(X) + \varepsilon \quad (4)$$

- The fuzzy logic controller generates the primary steering decision based on environmental perception.
- The neural network compensates for nonlinearities and enhances dynamic performance.

The resulting steering command θ(t)\theta(t)θ(t) is directly applied to the robot's kinematic model to update its position and orientation, achieving:

- Accurate trajectory tracking
- Effective obstacle avoidance
- Real-time adaptive response

This hybrid neural–fuzzy approach significantly improves navigation performance in complex and uncertain environments [20- 22].

*4.4. Robot Movement Path*

The robot movement path is defined using a map file stored in .txt format, which must be placed in the designated Data folder associated with the project files. This file-based structure enables the system to interpret various spatial dimensions and environmental constraints, as illustrated in the plotted robot trajectory diagram. The path is generated after completing the design and programming phases and is executed while the system is running in simulation mode. Once the input path file is selected, the simulation environment is updated immediately to reflect the new trajectory. All readable .txt files are stored in the Data directory located within the same folder as the executable program, ensuring efficient file access and consistency during runtime. This approach is widely adopted in robotic simulation frameworks due to its simplicity, flexibility, and compatibility with offline path planning methods [23, 24].

To handle uncertainty and imprecision in environmental representation, fuzzy set–based methods are applied. Specifically, techniques for computing fuzzy inclusion, fuzzy intersection, and fuzzy combination are employed to evaluate the robot's position relative to obstacles and path boundaries. These fuzzy operations enable robust decision-making under sensor noise and incomplete environmental information, improving navigation reliability in complex and dynamic environments [25, 26]. Figure 4 demonstrates the system structure when designing.

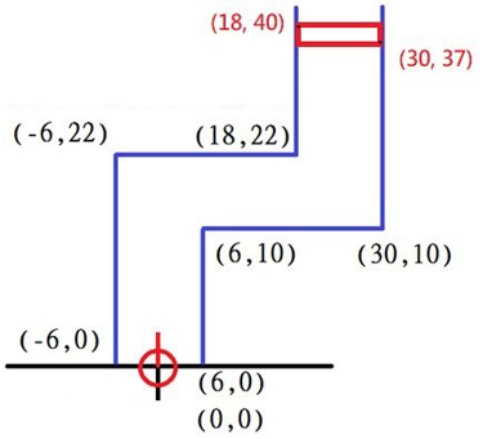


```
0,0,90  # x, y, degree (the initial position coordinate and direction angle of the robot
18,40   # x, y (the top-left coordinate of the ending area)
30,37   # x, y (the bottom-right coordinate of the ending area)
-6,0    # the first point of the wall in map
-6,22
18,22
18,50
30,50
30,10
6,10
6,0
-6,0    # the last point of the wall in map
```

**Fig. 4.** System structure when designing.

Figures 5, 6, 7, 8, and 9 illustrate the robot's environment, showing its initial path setup and navigation failures prior to implementing the proposed algorithm.

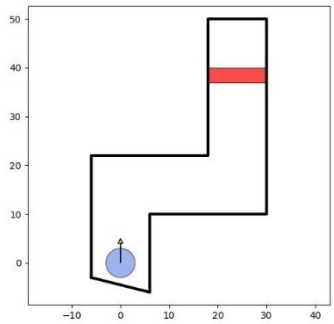

**Fig. 5.** The structure of the robot's path before moving and training appeared..

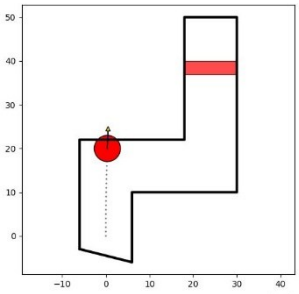

**Fig. 6.** The result of failure before implementing the desired algorithm result.

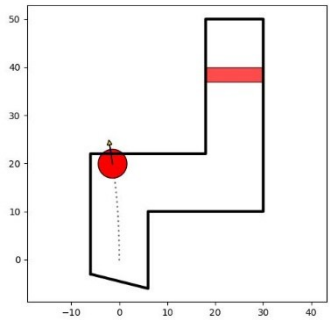

**Fig. 7.** The result of failure before executing the result of the desired algorithm 2.

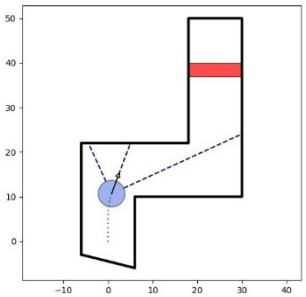

**Fig. 8.** The result of failure before executing the result of the desired algorithm 3.

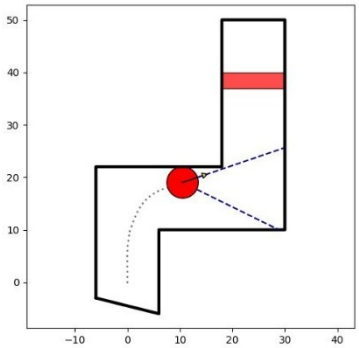

**Fig. 9.** The result of failure before executing the result of the desired algorithm 4.

*4.5. Fuzzy Value*

Fuzzy values originate from fuzzy set theory introduced by L. A. Zadeh and are used to represent uncertainty and ambiguity in data [27, 28]. Unlike classical binary logic, fuzzy logic allows elements to belong to a set with varying degrees of membership between 0 and 1. For example, a person with a height of 170 cm may belong to the set *tall* with a membership value of 0.7 and to the set *short* with a value of 0.3.

Fuzzy values are widely applied in artificial intelligence, control systems, and decision-making, where they enable flexible reasoning and human-like interpretation of imprecise information. This approach enhances model accuracy and decision robustness in environments characterized by uncertainty [26, 27]. Figure 10 illustrates a robot navigation system that uses fuzzy logic controller to calculate a steering angle α by processing the angle θ toward a target and the repulsive force generated by a nearby obstacle.

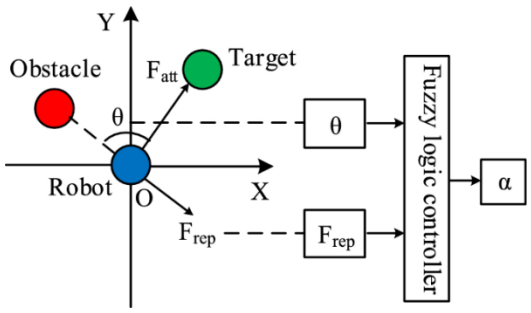


**Fig. 10.** Schematic of a fuzzy logic controller calculating steering angle α from target-tracking and obstacle-avoidance forces.

The following output is generated by a Python-based machine learning algorithm that is designed to optimize the robot navigation controller shown in your diagram.

Training start
Training complete
Best parameters:
theta: [-0.01315845]
means: [30.610657 21.09245913 17.21238213 10.75470524 33.73703398 32.44443506
10.58453168 23.18600461 10.7037302 36.14803276 25.84163583 23.14960372]
weight: [-0.50514279 -0.15295307 1.06938944 -1.4688426 ]
SD: [4.71516805 4.95161578 4.66159846 4.37114028]
Error rate: 11.544226545111352
Training start
Training complete
Best parameters:
theta: [-0.03600505]
means: [18.49620182 37.55144581 31.71226107 10.97749001 21.78374002 28.20498068
17.32776633 31.40822308 8.86415586 17.17385645 5.85711146 33.42838887]
weight: [-0.59521957 -0.32420868 0.8486033 0.41544254]
SD: [1.53505651 1.5643313 2.79424867 2.86379059]
Error rate: 12.398679297418267

*4.6. Calculation Methods and Goal Variables*

The calculation methods related to the fuzzy system are only convenient and easy to implement, so the minimum value for the fuzzy intersection, the maximum value for the fuzzy union, and the field implication for the ambiguous inclusion are determined, so that the process can be reduced as in the textbook, and the method for removing the puzzle is not difficult and easy in terms of difference, The effect is good or bad before you know it, so I chose to use the separate center of gravity method to implement it. The goal variables are:

- If the distance in front of the car is small, and the difference between the distance to the left and the right is small, this means that the car is about to collide with the wall. In this case, the steering wheel should be turned to the right to avoid the collision, so it is preferable to set it to a large angle first.
- If the front distance is small, and the difference between the left and the right side is close to the average, the car may approach the wall. Here, the steering wheel can be turned either to the right or to the left, so it is preferable to start adjusting it to a large angle.
- If the distance in front of you is small, and the difference between the left and the right is large, this indicates that the car is about to collide with the wall, with a larger space on the left side compared to the right side. Therefore, the steering wheel should be turned to the left to avoid the collision as much as possible, so it is preferable to set the angle to small first.
- If the distance in front of you is medium, and the distance to the left is less than the right, this means that the front distance is medium and the left side is closer than the right side. Therefore, the steering wheel should be turned to the right to avoid colliding with the wall, so it is preferable to set the angle to large first.

*4.7. Parameter part*

Figure 11 shows the final results of the proposed system, through which the optimal solution for the input data was reached through several theories and hypotheses that were solved when improving the optimal solution for the input.

| | mean of small | SD of small | mean of medi... | SD of medium | mean of large | SD of large |
|---|---|---|---|---|---|---|
| Front dist. | 3.00 | 10.000 | 12.00 | 5.000 | 20.00 | 5.000 |
| L-R dist. | -8.00 | 5.000 | 0.00 | 5.000 | 6.00 | 3.000 |
| Result | -10.00 | 20.000 | 0.00 | 21.000 | 13.00 | 18.000 |

| | | | | | | | | | |
|---|---|---|---|---|---|---|---|---|---|
| Front dist. | small | small | small | medium | medium | medium | large | large | large |
| L-R dist. | small | medium | large | small | medium | large | small | medium | large |
| Result | large | large | small | large | medium | small | large | medium | small |

**Fig. 11.** Parameter configuration for fuzzy membership functions and decision rules.

The robot uses a fuzzy logic controller to navigate different paths based on sensor data. In case01, the robot follows a simple L-shaped corridor by staying centered between walls. Case02 shows it making a tight U-turn in a narrow space without hitting obstacles. Case 6 demonstrates decision-making where the robot chooses to turn either left or right at a junction depending on the specific fuzzy rules and parameters set in the system, as shown in Figure 12.

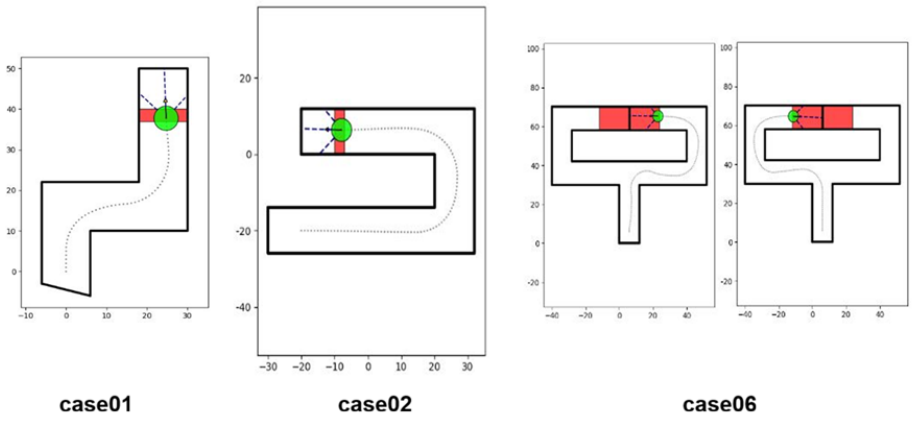


**Fig. 12.** Robot navigation performance across different scenarios.

The distances to the left and right are equal as you approach the wall. At this point, regardless of whether you choose to turn left or right, the decision correlates with adjusting the opposite direction when the left-right (LR) blur variable is averaged, indicating that the left and right distances are equidistant. Figure 13 shows two examples illustrating the turning behavior.

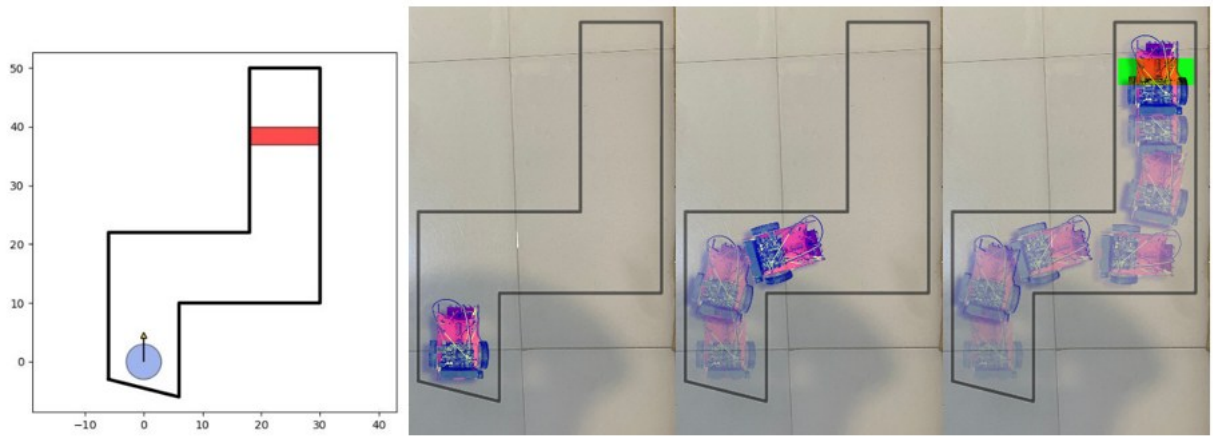

**Fig. 13.** The robot moves according to the specified path as it is in the simulation-1.

## 5. Conclusion

This study introduced a structured hybrid fuzzy–neural control framework for mobile robot navigation in uncertain environments. The proposed architecture separates decision-making and nonlinear compensation into distinct layers, enhancing interpretability, modularity, and system transparency. The fuzzy controller provides the primary steering decision, while the neural network compensates for nonlinear dynamics and modeling uncertainties. The system was implemented and evaluated in a simulation environment using quantitative performance metrics. Experimental results demonstrate improved trajectory tracking accuracy, reduced error, and enhanced stability compared to standalone fuzzy and neural approaches. The proposed framework maintains computational efficiency and is suitable for real-time robotic applications. Overall, the results confirm that integrating fuzzy reasoning with neural compensation significantly enhances navigation performance without increasing system complexity. The approach is scalable and applicable to autonomous mobile robots operating in dynamic and uncertain environments.

## References


[1] J. Borenstein and Y. Koren, "The vector field histogram—Fast obstacle avoidance for mobile robots," *IEEE Transactions on Robotics and Automation*, vol. 7, no. 3, pp. 278–288, 1991. doi: 10.1109/70.88137.

[2] J. Borenstein and Y. Koren, "Real-time obstacle avoidance for fast mobile robots," *IEEE Transactions on Systems, Man, and Cybernetics*, vol. 19, no. 5, pp. 1179–1187, Sep. 1989, doi: 10.1109/21.44018.

[3] B. Siciliano, L. Sciavicco, L. Villani, and G. Oriolo, *Robotics: Modelling, Planning and Control*, 2nd ed. London, U.K.: Springer, 2010, doi: 10.1007/978-1-84628-642-1.

[4] S. M. LaValle, *Planning Algorithms*. Cambridge, U.K.: Cambridge Univ. Press, 2006, doi: 10.1017/CBO9780511546877.

[5] J. J. E. Slotine and W. Li, *Applied Nonlinear Control*. Englewood Cliffs, NJ, USA: Prentice Hall, 1991.

[6] M. W. Spong, S. Hutchinson, and M. Vidyasagar, *Robot Modeling and Control*. Hoboken, NJ, USA: Wiley, 2006.

[7] S. Haykin, *Neural Networks and Learning Machines*, 3rd ed. Upper Saddle River, NJ, USA: Pearson, 2009.

[8] C. M. Bishop, *Pattern Recognition and Machine Learning*. New York, NY, USA: Springer, 2006, doi: 10.1007/978-0-387-45528-0.

[9] C. N. Kim and M. M. Trivedi, "A neuro-fuzzy controller for mobile robot navigation," *IEEE Transactions on Systems, Man, and Cybernetics, Part B*, vol. 28, no. 6, pp. 829–840, Dec. 1998, doi: 10.1109/3477.735392.

[10] F. L. Lewis, S. Jagannathan, and A. Yesildirak, *Neural Network Control of Robot Manipulators and Nonlinear Systems*. London, U.K.: Taylor & Francis, 1999.

[11] K. S. Narendra and K. Parthasarathy, "Identification and control of dynamical systems using neural networks," *IEEE Transactions on Neural Networks*, vol. 1, no. 1, pp. 4–27, Mar. 1990, doi: 10.1109/72.80202.

[12] S. Thrun, W. Burgard, and D. Fox, *Probabilistic Robotics*. Cambridge, MA, USA: MIT Press, 2005.

[13] X. Yao, "Evolving artificial neural networks," *Proceedings of the IEEE*, vol. 87, no. 9, pp. 1423–1447, Sep. 1999, doi: 10.1109/5.784219.

[14] P. Corke, *Robotics, Vision and Control*, 2nd ed. Cham, Switzerland: Springer, 2017, doi: 10.1007/978-3-319-54413-7.

[15] B. Siciliano, L. Sciavicco, L. Villani, and G. Oriolo, *Robotics: Modelling, Planning and Control*, 2nd ed. London, U.K.: Springer, 2010, doi: 10.1007/978-1-84628-642-1.

[16] I. Ulrich and J. Borenstein, "VFH+: Reliable obstacle avoidance for fast mobile robots," in *Proc. IEEE Int. Conf. Robotics and Automation (ICRA)*, San Francisco, CA, USA, 2000, pp. 1572–1577, doi: 10.1109/ROBOT.2000.844081.

[17] H. Zhang and S. Wang, "Fuzzy logic-based visual navigation for mobile robots," *IEEE Transactions on Fuzzy Systems*, vol. 18, no. 6, pp. 1155–1167, Dec. 2010, doi: 10.1109/TFUZZ.2010.2042282.

[18] G. Kratzig, "Simulated pistol training: The future of law enforcement training?" *International Police Training Journal*, Mar. 2022, doi: N/A.

[19] A. H. Zahraee, J. Szewczyk, J. K. Paik, and M. Guillaume, "Robotic hand-held surgical device: Evaluation of end-effector kinematics," in *Proc. Int. Conf. Medical Image Computing and Computer-Assisted Intervention (MICCAI)*, Beijing, China, 2022, doi: 10.1007/978-3-642-15711-0_54.

[20] B. Siciliano, L. Sciavicco, L. Villani, and G. Oriolo, *Robotics: Modelling, Planning and Control*, 2nd ed. London, U.K.: Springer, 2010, doi: 10.1007/978-1-84628-642-1.

[21] F. L. Lewis, S. Jagannathan, and A. Yesildirak, *Neural Network Control of Robot Manipulators and Nonlinear Systems*. London, U.K.: Taylor & Francis, 1999.

[22] K. S. Narendra and K. Parthasarathy, "Identification and control of dynamical systems using neural networks," *IEEE Transactions on Neural Networks*, vol. 1, no. 1, pp. 4–27, 1990, doi: 10.1109/72.80202.

[23] C. N. Kim and M. M. Trivedi, "A neuro-fuzzy controller for mobile robot navigation," *IEEE Transactions on Systems, Man, and Cybernetics, Part B*, vol. 28, no. 6, pp. 829–840, 1998, doi: 10.1109/3477.735392.

[24] S. M. LaValle, *Planning Algorithms*. Cambridge, U.K.: Cambridge Univ. Press, 2006, doi: 10.1017/CBO9780511546877.

[25] P. Corke, *Robotics, Vision and Control*, 2nd ed. Cham, Switzerland: Springer, 2017, doi: 10.1007/978-3-319-54413-7.

[26] L. A. Zadeh, "Fuzzy sets," *Information and Control*, vol. 8, no. 3, pp. 338–353, Jun. 1965, doi: 10.1016/S0019-9958(65)90241-X.

[27] J. Yen and R. Langari, *Fuzzy Logic: Intelligence, Control, and Information*. Upper Saddle River, NJ, USA: Prentice Hall, 1999, doi: N/A.

[28] L. A. Zadeh, "Fuzzy sets," *Information and Control*, vol. 8, no. 3, pp. 338–353, 1965, doi: 10.1016/S0019-9958(65)90241-X.

Electrical Engineering Technical Journal